BNL-223670-2022-JAAM

U-Pb Geochronology and Stable Isotope Geochemistry of Terrestrial Carbonates, Lower Cretaceous Cedar Mountain Formation, Utah: Implications for Synchronicity of Terrestrial and Marine Carbon Isotope Excursions

E. Gulbranson, R. Tappero

To be published in "GEOSCIENCES"

October 2022

Photon Sciences

Brookhaven National Laboratory

U.S. Department of Energy

USDOE Office of Science (SC), Basic Energy Sciences (BES) (SC-22)

DISCLAIMER

geosciences

MDPI

Article

U–Pb Geochronology and Stable Isotope Geochemistry of Terrestrial Carbonates, Lower Cretaceous Cedar Mountain Formation, Utah: Implications for Synchronicity of Terrestrial and Marine Carbon Isotope Excursions

Erik L. Gulbranson [1,*], E. Troy Rasbury [2], Greg A. Ludvigson [3], Andreas Möller [4], Gregory A. Henkes [2], Marina B. Suarez [4], Paul Northrup [2], Ryan V. Tappero [5], Julie A. Maxson [6], Russell S. Shapiro [7] and Kathleen M. Wooton [2]

[1] Department of Geology, Gustavus Adolphus College, St. Peter, MN 56082, USA
[2] Department of Geosciences, Stony Brook University, Stony Brook, NY 11794, USA
[3] Kansas Geological Survey, University of Kansas, Lawrence, KS 66045, USA
[4] Department of Geology, University of Kansas, Lawrence, KS 66045, USA
[5] National Synchrotron Light Source-II, Brookhaven National Laboratory, Upton, NY 11973, USA
[6] Natural Sciences Department, Metropolitan State University, St. Paul, MN 55106, USA
[7] Earth and Environmental Sciences Department, California State University Chico, Chico, CA 95929, USA
* Correspondence: erikgulbranson@gustavus.edu

check for updates

Citation: Gulbranson, E.L.; Rasbury, E.T.; Ludvigson, G.A.; Möller, A.; Henkes, G.A.; Suarez, M.B.; Northrup, P.; Tappero, R.V.; Maxson, J.A.; Shapiro, R.S.; et al. U–Pb Geochronology and Stable Isotope Geochemistry of Terrestrial Carbonates, Lower Cretaceous Cedar Mountain Formation, Utah: Implications for Synchronicity of Terrestrial and Marine Carbon Isotope Excursions. *Geosciences* **2022**, *12*, 346. https://doi.org/10.3390/geosciences12090346

Academic Editors: Jesus Martinez-Frias and José Manuel Castro

Received: 23 June 2022
Accepted: 14 September 2022
Published: 17 September 2022

Publisher's Note: MDPI stays neutral with regard to jurisdictional claims in published maps and institutional affiliations.

Abstract: The terrestrial Lower Cretaceous Cedar Mountain Formation, Utah, is a critical archive of paleoclimate, tectonics, and vertebrate ecology and evolution. Early Cretaceous carbon cycle perturbations associated with ocean anoxia have been interpreted from this succession, as expressed in stable carbon isotopes. However, refining the timing of the observed stable isotope excursions remains a key challenge in understanding how marine anoxia affects the Earth system, and is ultimately recorded in the terrestrial realm. The geochronology and geochemistry of a terrestrial carbonate near the base of this succession, which potentially records the Ap7 global carbon isotope excursion, is studied here. Petrographic and geochemical analyses are used to test plausible mechanisms for U incorporation into the calcite lattice in this sample. Using these methods, the hypothesis that the incorporation of U was at or close to the timing of carbonate precipitation is evaluated. U–Pb geochronology of calcite indicates a plausible Early Cretaceous age. However, comparison of the new U–Pb ages of calcite with detrital zircon maximum depositional ages immediately beneath the studied sample indicates a disparity in the apparent sedimentation rates if both types of geochronologic information are interpreted as reflecting the timing of sediment deposition. The totality of data supports an early, and high-temperature, diagenetic timing of U incorporation, with potential for minor leaching of U in subsequent fluid–rock interaction. The most likely mechanism for U transport and immobilization in these samples is hydrothermal fluid–rock interaction. Therefore, the radiometric ages, and corresponding stable isotope composition of U-bearing carbonate domains in this sample, indicate early subsurface fluid–rock interactions and not a record of atmosphere–soil geochemical reactions.

Keywords: U–Pb geochronology; diagenesis; calcrete; palustrine; Early Cretaceous; clumped isotope

1. Introduction

The Cretaceous represents a time of pronounced oceanic and atmospheric change, resulting in fluctuating climate states and episodic global ocean anoxia and localized dysoxia [1–5]. Volcanism-induced perturbations to the global carbon cycle were a potential driver of these global changes, as the emergence of several large igneous provinces (LIPs) [6], notably the Ontong Java–Manihiki LIP [7], coincided with intervals of ocean anoxia [8]. The coincidence of LIP volcanism and Cretaceous ocean anoxic events (OAE) is

well-documented in the increasingly refined Cretaceous geologic time scale [8–10]. The timing of ocean anoxia and paleoclimate perturbations/ecologic change on land are gaining increasing fidelity through isotope analysis of terrestrial-derived fossil plant material [11–15], and through chemostratigraphic comparisons between fully terrestrial and marine successions [16–22]. However, the necessity of calibrating the age of marine and terrestrial stratigraphic successions during OAEs via high-precision radiometric dating has hindered precise connections between observed shifts in stable carbon isotopes in terrestrial successions with the well-known marine isotopic time series changes. This study adds additional insight into the connections between terrestrial environments, and perhaps climatic change, during the earliest global OAE of the Cretaceous (The Aptian OAE-1a, "Selli Event") using a combined radioisotope, petrographic, geochemical, and stable isotope investigation of terrestrial carbonates from the Cedar Mountain Formation.

The Cedar Mountain Formation is a Lower Cretaceous succession of terrestrial strata in the four corners region of the western United States, cropping out in Utah and correlative units in Wyoming and western Colorado [23] (Figure 1). This succession is gaining increasing prominence for the rich record of vertebrate fossils at key evolutionary junctions in Ornithischia [24,25], and the potential paleoclimate and geochemical records of terrestrial change coincident with marine OAEs [19]. The Cedar Mountain Formation is subdivided into five lithostratigraphic members (Figure 2), not all of which are preserved everywhere. In order from oldest to youngest these are: the Buckhorn Conglomerate, the Yellow Cat member, the Poison Strip sandstone, the Ruby Ranch Member, and the Mussentuchit member. The Yellow Cat member and Poison Strip sandstone are regarded as time equivalent to all of or part of the Buckhorn Conglomerate [18] and occur between the Colorado and Green rivers in southeastern Utah (Figure 1A). The Poison Strip and Ruby Ranch members of the Cedar Mountain Formation plausibly record a chemostratigraphic expression of global climate change during the first ~1.2 myr global OAE of the Cretaceous, OAE-1a [18]. Therefore, the age and diagenetic history of carbonates from the Poison Strip and Ruby Ranch members are the focus of this study.

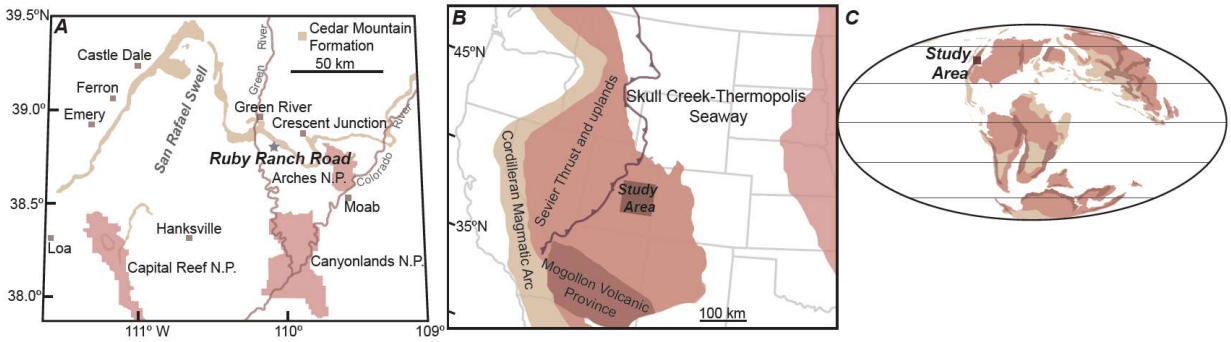

Figure 1. Maps of the field locations (after [19]). (**A**) Outcrop map of the Cedar Mountain Formation (shaded region around the San Rafael Swell and elsewhere) in present-day Utah. (**B**) Paleogeographic reconstruction of the study area with respect to the Sevier Foreland Basin and the Skullcreek-Thermopolis Seaway. (**C**) Global paleogeography during the early Aptian with the location of the study area indicated by the square symbol. Color gradient reflects general areas of low–high relief (light to dark colors, respectively).

Detrital zircon U–Pb geochronology has been used to draw important inferences to the tectonic and erosion controls on sediment supply and deposition of the Cedar Mountain Formation in the foreland basin of the Sevier orogen [26,27]. In the absence of conventional single crystal ID-TIMS or detrital zircon analyses of sedimentary strata, non-conventional approaches of applying (laser ablation inductively coupled plasma mass spectrometry (LA-ICP-MS) analysis to paleosol zircon crystal yielded promising U–Pb age populations [21], as well as the U–Pb analysis of carbonates, which is reported herein, and from [18]. These new geochronologic methods have greatly improved the resolution of time recorded in these

strata, allowing terrestrial–marine geochemical correlations for significant Early Cretaceous climate phenomena such as the Valanginian "Weissert Event" [13,28,29] for the Yellow Cat member with a zircon crystallization age of 136.3 ± 1.3 Ma [21] and 135.10 ± 0.3, 0.31, 0.34 Ma [30,31]. The overlying Poison Strip member produced a carbonate (calcite) U–Pb age of 119.4 ± 2.6 Ma [18]. Volcanic ashes in the uppermost Mussentuchit Member of the Cedar Mountain Formation have yielded precise $^{40}Ar/^{39}Ar$ (sanidine) ages of the mid-Cretaceous, 98.39 ± 0.07 Ma [30], and mean ages ranging from 98.5 ± 0.6 Ma to 96.7 ± 0.5 Ma [32]. The Mussentuchit member also yields inferred maximum depositional ages (MDA) of between 96–94 ± ~1.3 Ma based on detrital zircon U–Pb analyses using LA-ICP-MS, as well as two chemical abrasion thermal ionization mass spectrometry (CA-TIMS) ages of 95.64 ± 0.11 Ma and 99.68 ± 0.12 Ma [33]. The revised geochronology reported herein is focused on the nature and timing of U complexation in terrestrial carbonates from the Poison Strip member of the Cedar Mountain Formation to elucidate the age of the lowermost sections of the Cedar Mountain Formation. This carbonate geochronology technique stems from the pioneering Pb-Pb geochronology work of Moorbath et al. [34] and U–Pb analyses of Smith and Farquhar [35], and has been shown to be reliable in comparison to more conventional dating techniques [36].

Over a decade of terrestrial carbonate stable isotope measurements from the Yellow Cat–Ruby Ranch members of the Cedar Mountain Formation has resulted in a large range of $\delta^{18}O$ values (−3‰ to −18‰ VPDB), including a significant number of diagenetic carbonates with $\delta^{18}O$ values < 9‰ [18,19,22,37–40] (Figures 2 and 3). Determining which carbonate components preserve an authigenic isotope signal has been challenging as it is evident that paleoclimate/environmental change produced varying meteoric water $\delta^{18}O$ values, which overlap with some components that reflect hydrothermal alteration during burial [19]. In addition, plausible variations in atmospheric CO_2 concentrations [19] and variations in paleoecology [41,42] may have led to similarly high variance in measured $\delta^{13}C$ values. Furthermore, the specter of complete isotopic overprinting through later stage diagenesis and hypogene hydrocarbon migration, borne out through two independent paleotemperature estimates [22,40], remains plausible for the majority of this stratigraphic succession. Nevertheless, through detailed petrographic analysis and microsampling for stable isotopes in space and time, more detailed and confident assessments of paleoevaporation extents and ancient carbon cycling have been made [19,22,39]. A compilation of all available stable oxygen and carbon isotope data for the Yellow Cat and Ruby Ranch members of the Cedar Mountain Formation (see Supplementary Material) indicate that $\delta^{18}O$ values have an order of magnitude greater variation than $\delta^{13}C$ values, and lack an "inverted-J" signature of regional isotopic resetting during burial diagenesis [43]. Rather, carbonate cement stratigraphy reveals subsets of the overall data set that may reflect early meteoric diagenesis conditions that are distinct from the larger range of $\delta^{18}O$ values (more negative than −9‰) with relatively invariant $\delta^{13}C$ values indicating later stage isotope exchange during fluid flow and hydrocarbon migration through Cedar Mountain Formation strata [40]. Of the more authigenic carbonate domains, variable slopes of covariant $\delta^{18}O$ and $\delta^{13}C$ values are indicative of changing evaporative conditions and soil productivity through time [19,22,39]. A nominal $\delta^{18}O$ value of between −9 to −8‰ is indicative of "meteoric calcite lines" for this region [29,37]. However, the meteoric calcite line $\delta^{18}O$ values change through time: (1) a shift to more negative values (ca. −15‰) within the Poison Strip member; (2) a progressive increase in meteoric calcite line $\delta^{18}O$ values in the Ruby Ranch member (ca. −8‰); and (3) a shift towards more negative $\delta^{18}O$ values in the upper part of the Ruby Ranch member (ca. −9 to −10‰). The meteoric calcite lines also display a range of $\delta^{13}C$ values from 2–3‰ between distinct meteoric calcite line $\delta^{18}O$ values, which indicates prominent variations in ecosystem productivity or equilibration with different paleoclimates, a conclusion supported by paleobotanical reconstructions of the paleoclimate in the Cedar Mountain Formation [41].

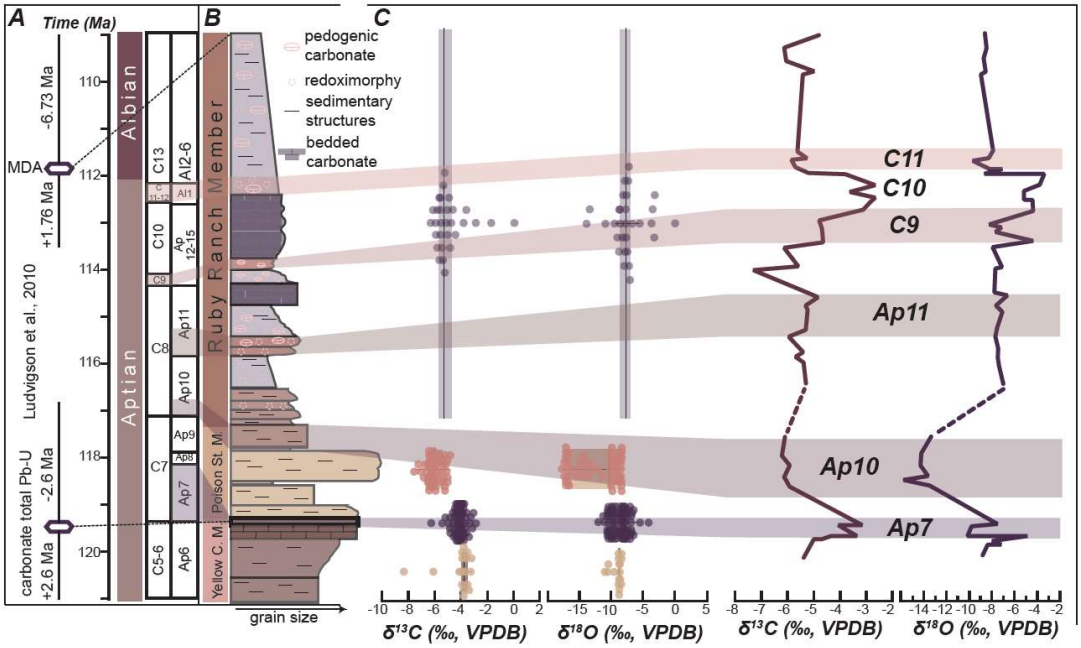

Figure 2. Summary of Cedar Mountain Formation strata discussed in this study and chemostratigraphic correlations. (**A**) Current radiometric constraints on the Yellow Cat, Poison Strip, and Ruby Ranch members, and marine-based carbon isotope stages. (**B**) Composite stratigraphic column including field areas on the eastern San Rafael Swell and the Paradox Basin. (**C**) Summary of C and O stable isotope compositions based on individual members within the Cedar Mountain Formation and chemostratigraphic trends (after [19,40]).

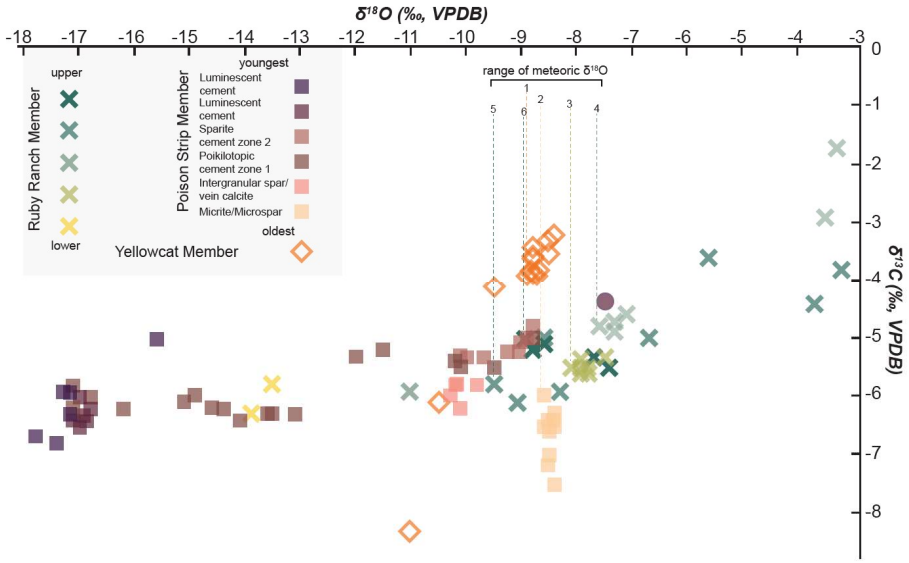

Figure 3. Summary of stable isotope data on carbonate materials in the Cedar Mountain Formation. Data are presented in stratigraphic order as well as inferred temporal sequence (e.g., cement stratigraphy of the Poison Strip member [40]). The Yellow Cat member data are from lacustrine oncoid material [37]. The overlying carbonate-cements sandstones of the Poison Strip member are from [40]. The overlying Ruby Ranch member pedogenic carbonate results are from [22]. Inferred meteoric calcite lines (MCLs) are shown for each of the data sets and numbered sequentially through time, with 1 being the oldest, and 6 being the youngest.

The stratigraphic variation of authigenic $\delta^{13}C$ values of terrestrial carbonates, palustrine, and calcrete carbonate further indicate pronounced excursions of $\delta^{13}C$ values through time. These excursions have been correlated to the stages of chemostratigraphic variation recognized in marine successions, and with the current U–Pb MDAs and carbonate U–Pb ages, indicate that these excursions are correlative to marine fluctuations in DIC and organic carbon burial [18,19]. However, revisions to the Cretaceous timescale [6,8] have created uncertainty in the exact timing of Cretaceous OAEs; for example, in the case of OAE-1a, shifting the timing of this event by ~6 myr. Refining the U–Pb-calibrated numeric timescale for the Cedar Mountain Formation, therefore, is critical to elucidating the connection between the terrestrial record of paleoclimate/paleoecologic change and the marine OAEs.

2. Geologic Setting

Intentionally ignored in the second half of the 20th century for geologic and paleontologic study because of the "lack of vertebrate fossils", the Cedar Mountain Formation in the 21st century is now known to be a pivotal archive for the evolution and biogeography of terrestrial vertebrates [24,44]. In addition, the lithostratigraphic position of the Cedar Mountain Formation is vital for understanding the unique pattern of basin evolution in the early stages of Sevier orogenesis [45]. This succession preserves an archive of terrestrial–marine teleconnections during the lilt of Early Cretaceous OAEs, climate and hydrologic cycle changes, in the form of their attendant stable isotope perturbations [46,47]. Thus, an intense interest has emerged in the last decade for refining the numerical age control of this slightly drab to variegated collection of mudstone, carbonate, and sandstone.

The Cedar Mountain Formation represents deposition in the transition to, and acme of, thick-skinned thrusting that generated the Sevier foreland basin [45,48,49]. The origin of the foreland basin-style subsidence and geometry of the sedimentary wedge adjacent to the Sevier orogenic belt occurred during the Aptian [26,48], which indicates that the Yellow Cat member of the Cedar Mountain Formation and the Buckhorn Conglomerate most likely record deposition in the incipient stages of compressional tectonism in the region. The spatial limitations of the Yellow Cat member, within the Paradox Basin, along with increases in isopach thickness of Lower Cretaceous strata in this region, indicate that halokinesis was likely an important local control on subsidence in the study area [23,45].

The Buckhorn Conglomerate is a predominantly lithic extraformational clast-supported conglomerate with gravel bedforms and sheet-like deposits confined to distinct channelized geometries. Minor laterally discontinuous lithic arenite/wacke bedsets occur within this unit with preservation of terrestrial vertebrate fossils; however, laterally correlative overbank facies are uncommon, as the channel systems are bound laterally against 5th order erosional surfaces (as defined by [50]). Vertebrate fossils have been recovered from the arenitic/wacke portion of this rock unit [23]. Detrital zircon U–Pb analyses indicate a successive change in chronofacies upsection, with a distinct Pennsylvanian–Jurassic age of clasts indicative of erosional unroofing of the Sevier orogenic belt and subsequent transport of that sediment into the alluvial–fluvial systems of the Buckhorn Conglomerate [26]. However, the broad areal extent (600 km along the length of the conglomeratic fluvial system) of the Buckhorn Conglomerate and its correlative units in Wyoming, Colorado, Montana, and Canada is indicative of regional uplift of the Sevier orogenic belt prior to the initiation of foreland basin-style subsidence [48,51]. Based on data-model comparisons of the slopes required for physical transport of gravel clasts in the Buckhorn Conglomerate, Heller and Paola [48] and Yingling and Heller [48] conclude that these sedimentary units record pre-thrust sheet tilting and initial erosion of bedrock and underlying strata, whereas the overlying units of the Cedar Mountain Formation record the progressive development of foreland basin-style subsidence in response to loading of the crust from thrusting during the Sevier orogeny.

The Yellow Cat member is a laterally discontinuous unit at the basin-scale, attaining a maximum thickness of ~50 m, occurring only between the Green and Colorado rivers

in southeastern Utah, and consists of variegated mudstones displaying pedogenic iron nodules [23], sand sheet, sediment gravity flow, and sandy bedform elements [52], and an uppermost terrestrial carbonate succession [53]. In terms of lithofacies abundance, the Yellow Cat member is predominantly overbank fine material with an increasing abundance of pedogenic carbonate up section. The uppermost part of the Buckhorn Conglomerate at Woodside Anticline in the eastern limb of the San Rafael Swell contains oncoids on gravel and dinosaur/wood clasts [37], indicating a continuity of depositional/paleoenvironmental settings between the uppermost portions of the Buckhorn Conglomerate and Yellow Cat member depositional systems. Consistent with this interpretation, the Yellow Cat member may represent an extensive period of overbank deposition adjacent to the prominent channel systems of the Buckhorn Conglomerate. However, the lowermost hydromorphic paleosols of the Yellow Cat member have been regarded as a continuation of the Brushy Basin Member of the Morrison Formation [54]. Kirkland et al. [23] interpret these paleosols as part of the Cedar Mountain Formation based on an interpretation of a "wet" paleoclimate that stands in contrast to more arid paleoclimates of older and younger strata [54,55], and set the unconformable contact between the Jurassic and Cretaceous at the base of this succession. The climate-based interpretation of Kirkland et al. [23] demands a more rigorous assessment of the bio-/chronostratigraphy of the basal portion of the Cedar Mountain Formation to further clarify these discrepancies. The uppermost Yellow Cat member displays a laterally discontinuous succession of multistage pedogenic carbonate development [53]. These carbonates range in thickness from 1 m up to several meters and occur prominently as ridges at the Ruby Ranch Road locality [23]. The extensive pedogenic carbonates are capped by a laminated, brecciated, and chert-cemented terrestrial carbonate, interpreted to reflect palustrine deposition and pedogenesis [19]. The palustrine carbonate yielded a total U–Pb age of 119.4 ± 2.6 Ma [18], and this deposit is the focus of this study.

The Poison Strip member displays facies elements of sand and gravel bedforms, and downstream accretion elements, as well as a lithofacies abundance that is dominated by sandstones [24,40]. The fluvial system of the Poison Strip Member extends across the Sevier Foreland Basin [56–58] and is the lowermost laterally continuous subdivision of the Cedar Mountain Formation. Thus, in contrast to the Yellow Cat member, which may record overbank sedimentary systems coeval to the Buckhorn Conglomerate fluvial system, the Poison Strip member represents a reorganization of the fluvial system of the Sevier Foreland Basin. Furthermore, halokinetic fault movements of the Paradox Basin, which may have locally controlled the sedimentary systems of the fluvio-lacustrine Yellow Cat member, are interpreted to have had little impact on the fluvial sedimentary systems of the Poison Strip member, as lateral lithofacies variations occur independent of location with respect to the Paradox Basin [23]. The Poison Strip member, however, ranges in thickness from 2 m to ~20 m.

The Ruby Ranch member occurs at every location where the Cedar Mountain Formation is preserved [23]. Sand bedforms, gravel bars, downstream accretion elements, and a distinct ribbon-channel morphology are observed in the in-channel lithofacies of the Ruby Ranch member. Moreover, weathering and erosion of these rock units have superimposed the ribbon-channel morphology as relatively continuous ridge lines of exhumed paleochannels. Overbank lithofacies include abundant variegated siltstones and illite-bearing mudstones, displaying very common pedogenic calcite nodules [18,19,22,59] and less common bedded carbonate [19,60]. By proportion, the Ruby Ranch member is predominantly overbank lithofacies and is often recognized in the field on the basis of ~10–100 m thick successions of carbonate-bearing variegated siltstones and mudstones, contrasting against the sandstone lithofacies below and smectite-bearing mudstone-dominated succession of the overlying Mussentuchit member lacking pedogenic carbonate [38], or the quartzose sandstone lithofacies of the Naturita Formation, where the Mussentuchit member is absent. The thickness of the Ruby Ranch member increases in a roughly SW–NE direction, reaching a maximum thickness in the northern areas of the San Rafael Swell [23,61]. The Paradox Basin, however, preserves a vertical facies association of Ruby Ranch member strata,

with basal sandstone in-channel lithofacies underlying a silt- and mudstone-dominated succession interpreted as lacustrine facies [23,62].

The Mussentuchit member occurs primarily along the western flank of the San Rafael Swell [25,61,63]. This unit is recognized as a succession of fossiliferous mudstones containing abundant smectite-group minerals and coal [25]. A basal lag deposit of gravelly sand bedforms separates the Mussentuchit member from the underlying Ruby Ranch member [23,25]. The first systematic macrofloral record from the Cedar Mountain Formation was recovered from the Mussentuchit member, the "Soap Wash flora" [41,42], an assemblage which is angiosperm-dominated. Moreover, the macroflora recovered from the Mussentuchit member indicates that a diverse woody dicot forested ecosystem existed in this region that contained diverse plant traits such as leaf longevity [42].

3. Materials and Methods

3.1. The Sample

The carbonate sample studied herein was collected in 2003 from the uppermost Yellow Cat member of the Cedar Mountain Formation. This sample was studied in the field and collected from the Ruby Ranch Road field locality (38.854525° N, 109.970845° W). The sample is derived from a thick-bedded, laminated micritic limestone. At the hand sample-scale, cements within the limestone are either microsparite, sparite, or chert. Laminations within the limestone display a distinct transition from brecciated laminations at the base of the sample, with numerous cements, to laminations that display lateral continuity across the limestone, with minor brecciation locally. The sample is interpreted to reflect a palustrine depositional environment on the basis of the laminated bedding character, reflecting episodes of carbonate deposition; with brecciation of the lower laminae indicating subaerial exposure between two or more phases of limestone deposition [19].

3.2. Petrographic Investigations

Carbonate petrography was assessed via optical microscopy and cathodoluminescence (CL) at the Kansas Geological Survey. An Olympus BX51 petrographic microscope with a digital 10.5 Mpx Olympus SC100 color camera under paired plane-polarized and cross-polarized illumination was used to characterize the carbonate mineralogy and generate photomicrograph images. A CL imaging analysis was used to assess zonation and cement stratigraphy within the samples. A Relion Industries Reliotron III cold-cathode chamber, with operating conditions consisting of a rarified helium atmosphere at 50 milliTorr, an accelerating voltage of 10 kV, and a beam current of 0.5 mA, was used for imaging. Macroscale imaging through the 50 mm top window of the chamber was carried out using a 16 Mpx Canon EOS SL1 DSLR camera with a macro lens suspended over the CL chamber. Microscale imaging was carried out with the CL chamber mounted on a modified Olympus BX41 compound microscope using a Peltier-cooled 17 Mpx Olympus DP73 color camera. Imaging modes included transmitted light, reflected light (RL), and CL. Macroscale imaging was used to quickly scan thin and thick sections for the identification of microscopic domains of special interest. Paired microscopic RL and CL images were also collected to map microsampling targets from micropolished thick sections at sub-millimeter scales.

3.3. Uranium Chemistry and Spatial Distribution

Autoradiography was used to generate spatial maps of radionuclide concentration prior to laser ablation and synchrotron analysis at the University of Minnesota. Slabbed and polished samples of carbonate were placed on a phosphor imaging plate [64]. The imaging plate was a film of photostimuable barium fluoro bromide doped with Eu^{2+}, and overlain with a protective coating. The slabbed samples interacted with the plate for 30 d in a darkroom environment, where any ionizing radiation energy from the sample was stored in the phosphor crystals. After 30 d, the samples were removed and the plate was imaged by scanning the plate with a laser (λ = 400 nm), releasing the stored ionizing radiation energy as light which was captured by a photomultiplier tube (1000 V potential). The

light intensity is proportional to the concentration of radionuclides in a sample in direct contact with the plate. The phosphor images were overlain onto photographic images of the samples to locate regions of high radionuclide concentration.

Synchrotron X-ray Fluorescence (XRF) mapping at the National Synchrotron Light Source (NSLS) X26A and NSLS II XFM hard X-ray beam lines show the relationships between U and other elements. XRF maps were made by moving the sample across the beam, and the fluorescence was recorded by detectors. These maps were made at 17.3 keV to be above the binding energy for U. Areas of elevated U concentrations were selected for U X-ray Adsorption Near Edge Structure (U-XANES) analyses at the U L_3 edge (the excitation of an electron in the 2p subshell to an unfilled d subshell, where L_3 has the highest intensity signal at the lowest energy). This method scans in energy from just below to above the U L3 edge position, and the position of the edge is indicative of the oxidation state of U in the sample [65].

3.4. Uranium–Lead Geochronology

Laser ablation inductively coupled plasma (LA-ICP-MS) analyses were conducted at the Facility for Isotope Research and Student Training (FIRST) at Stony Brook University (SBU) and at the University of Kansas. At SBU, a 213 UV New Wave laser system coupled to an Agilent 7500cx quadrupole ICP-MS was used (Table 1). While the mixed gas was typically set at 0.85 L/min, it was also used to tune to minimize oxides and doubly charged ions and can range between 0.75 and 1.1 L/min. Additionally, the torch in/out position was adjusted to maximize signal and minimize oxides and doubly charged ions. U/Pb ratios were analyzed using spot analyses. ^{238}U, ^{232}Th, and ^{208}Pb, ^{207}Pb, and ^{206}Pb were collected sequentially for 0.1 s with 30 s ablation time and a 120 µm spot. Unknowns were bracketed by 5 reference material spots (both NIST612 soda glass, and WC-1 calcite) and 2 of each of the reference materials were analyzed between 10 unknown spots. A typical session had 30 unknown spots, 16–20 spots of each reference material, and a secondary standard such as Barstow [66]. The WC-1 calcite reference material [65] was used to calculate U/Pb, and NIST612 was used for Pb isotope fractionation correction and for approximating element concentrations using signal intensity. U–Pb data were processed with the U–Pb geochronology data reduction scheme (DRS) [67] and trace elements were processed with the trace element DRS [68]. After data reduction, IsoplotR [69] was used to plot U–Pb data on Tera–Wasserburg-type Concordia plots.

Table 1. Laser ablation instruments and parameters used in this study (Stony Brook University).

Instrument	Settings and Running Parameters
New Wave Research UP-213 Laser	Fluence: 0.75–1.20 J cm^{-2} Repetition Rate: 20 Hz Ablation duration for spots: 30 s Sample movement rate for maps: 20 microns/s Spot diameter: 120 microns Carrier gas: 100% He in cell—1.21 L/min Makeup gas: Ar—0.85–0.9 L/min (tuned to optimize signal and minimize doubly charged ions and oxides (sourced from Agilent)
Agilent 7500cx Quadrupole ICP-MS	Sample introduction: ablation aerosol via conventional tubing RF power: 1250 W Detection system: Dual-mode electron multiplier Masses Measured: ^{238}U, ^{232}Th, ^{208}Pb, ^{207}Pb, ^{206}Pb, ^{88}Sr, ^{43}Ca, ^{28}Si, ^{24}Mg

LA-ICP-MS analyses were conducted at the University of Kansas with a Thermo Scientific Element2 ICP-MS attached to a Photon Machines Analyte.G2 193 nm ArF excimer LA system (see Table 2 for operating parameters). Circular spots of 130 µm diameter were ab-

lated with the laser at 2.7 J cm^{-1} fluency and 10 Hz repetition rate. The ablated material was carried to the ICP in He carrier gas at 1.01 L min^{-1} and blended, 20 cm before entering the ICP-MS, with Ar carrier gas at 1.1 L min^{-1}. Isotope fractionation for Pb, laser-induced fractionation, and calibration drift were corrected by bracketing measurements of unknowns with NIST614 glass using the U_Pb_Geochronology3 data reduction scheme for the IOLITE software package [66]. Data produced with these programs was then exported to Microsoft Excel for correction of U/Pb and uncertainty propagation (pers comm. A. Kylander-Clark), using the carbonate reference materials Duff Brown Tank limestone for calibration and WC-1 calcite for validation. Tera–Wasserburg concordia plots were produced using the ISOPLOT version 4.12 macro for Microsoft Excel.

Table 2. Laser ablation instruments and parameters used in this study (University of Kansas).

Instrument	Settings and Running Parameters
Arf excimer 193 nm, Photon Machines Analyte G2, Atlex300	Fluence: 2.7 J cm^{-2} Repetition Rate: 10 Hz Ablation duration for spots: 30 s Sample movement rate for maps: 20 microns/s Spot diameter: 130 microns Carrier gas: He—1.1 L/min, Ar—1.35 L/min (two-volume cell) Makeup gas: Ar—0.85–0.9 L/min (tuned to optimize signal and minimize doubly charged ions and oxides (sourced from Agilent)
Thermo Element2 magnetic sector field ICP-MS	Sample introduction: ablation aerosol via conventional tubing RF power: 1350 W Detection system: single detector, counting Masses Measured: ^{238}U, ^{232}Th, ^{208}Pb, ^{207}Pb, ^{206}Pb

The lack of knowledge of the initial U activity ratio ($^{234}U/^{238}U$) of the U-rich fluids [70] is potentially an issue with U–Pb carbonate analyses. High $^{234}U/^{238}U$ activity produces unsupported ^{206}Pb that would cause age calculations to be too old, and this effect has been well documented for calcite of Pleistocene age [71]. However, given the Cretaceous age of the limestone from this study, it would be nearly impossible to measure any residual disequilibrium, and therefore we were unable to make any quantifiable correction for this effect. This potential bias is likely insignificant relative to the magnitude of reported uncertainties presented, and thus holds little potential to change the overall interpretation of ages and their geological significance. Isochron results presented here have a spread of MSWDs that range from ±1 to significantly greater than/less than 1 (over-dispersed). Modelled ages that were over-dispersed, i.e., ages not passing a chi-square test for age homogeneity, were treated with caution, but the ages were entirely consistent with better constrained isochrons.

3.5. Carbon and Oxygen Isotopic Compositions of Carbonate Minerals

Based on petrographic analysis, five discrete microfacies within the Cedar Mountain Formation sample were sampled to characterize carbon and oxygen stable isotope variation. The goal of this effort was to understand the relationship of the U-bearing carbonate component to other phases interpreted as representing primary calcite precipitation and various stages of secondary diagenetic alteration within this sample. These components were densely sampled ($n_{average}$ = 14.3) with 50 µm tungsten-carbide drill bits and analyzed via stable isotope ratio mass spectrometry at UC Davis and the University of Kansas. Calcite microsamples of between 20–30 µg were roasted in vacuo for 1 hr at 380 °C to remove organic materials and adsorbed CO_2. Roasted microsamples were reacted with anhydrous H_3PO_4 at 70 °C in an automated Kiel III device coupled to a ThermoFinnigan

MAT 252 isotope ratio mass spectrometer (University of Kansas, Lawrence, KS, USA) or a GVI Optima isotope ratio mass spectrometer (Stan Margolis Stable Isotope Laboratory, University of California Davis). Analytical precision was ±0.1‰ for $\delta^{13}C$ and $\delta^{18}O$ during the timeframe of analysis (2007–2009) based on repeated analysis of the secondary reference material UCD-SM92, and replicate microsamples (Table 3).

Table 3. Stable isotope results and carbonate domain.

$\delta^{18}O$ (VPDB)	$\delta^{13}C$ (VPDB)	Carbonate Domain	Cement Stratigraphy
−9.66	−3.80	Micrite	Stratum 1
−9.96	−3.83	Micrite	Stratum 1
−10.14	−3.82	Micrite	Stratum 1
−10.46	−3.79	Micrite	Stratum 1
−10.28	−4.09	Micrite	Stratum 1
−10.06	−3.87	Micrite	Stratum 1
−10.35	−4.08	Micrite	Stratum 1
−9.75	−3.82	Micrite	Stratum 1
−10.26	−3.79	Micrite	Stratum 1
−9.95	−3.56	Micrite	Stratum 1
−9.30	−3.26	Micrite	Stratum 1
−8.88	−3.71	Micrite	Stratum 1
−8.86	−3.62	Micrite	Stratum 1
−10.65	−4.56	Micrite	Stratum 3
−10.56	−4.59	Micrite	Stratum 3
−10.52	−4.53	Micrite	Stratum 3
−10.60	−4.46	Micrite	Stratum 3
−10.48	−4.32	Micrite	Stratum 3
−9.78	−4.06	Micrite	Stratum 3
−9.36	−4.24	Micrite	Stratum 3
−8.51	−3.93	Micrite	Stratum 3
−8.06	−3.80	Micrite	Stratum 3
−8.90	−3.92	Micrite	Stratum 3
−9.61	−4.00	Micrite	Stratum 3
−9.39	−3.73	Micrite	Stratum 3
−11.08	−4.82	Micrite	Stratum 4
−11.37	−4.91	Micrite	Stratum 4
−7.47	−3.81	Micrite	Stratum 4
−7.65	−4.12	Micrite	Stratum 4
−10.47	−4.78	Micrite	Stratum 4
−10.58	−4.34	Micrite	Stratum 4
−10.59	−4.34	Micrite	Stratum 4
−9.90	−5.41	Micrite	Stratum 4
−7.89	−3.94	Micrite	Stratum 4
−7.45	−3.33	Micrite	Stratum 4
−7.83	−3.83	Micrite	Stratum 4
−7.85	−3.97	Micrite	Stratum 4
−7.77	−4.08	Micrite	Stratum 4
−7.61	−4.14	Micrite	Stratum 4
−8.03	−4.1	Micrite	(Stratum 2) U-enriched
−8.26	−4.29	Micrite	(Stratum 2) U-enriched
−8.4	−4.26	Micrite	(Stratum 2) U-enriched
−8.56	−4.27	Micrite	(Stratum 2) U-enriched
−8.45	−4.24	Micrite	(Stratum 2) U-enriched
−8.48	−4.32	Micrite	(Stratum 2) U-enriched
−8.18	−4.1	Micrite	(Stratum 2) U-enriched
−8.08	−4.15	Micrite	(Stratum 2) U-enriched
−8.01	−3.91	Micrite	(Stratum 2) U-enriched
−8.38	−4.17	Micrite	(Stratum 2) U-enriched
−8.16	−4.14	Micrite	(Stratum 2) U-enriched
−7.89	−4.02	Micrite	(Stratum 2) U-enriched
−8.32	−4.17	Micrite	(Stratum 2) U-enriched
−8.07	−4.32	Micrite	(Stratum 2) U-enriched
−8.1	−4.12	Micrite	(Stratum 2) U-enriched
−8.05	−4.14	Micrite	(Stratum 2) U-enriched
−6.88	−3.4	Micrite	Stratum 1
−7.05	−4.04	Micrite	Stratum 1

Table 3. *Cont.*

$\delta^{18}O$ (VPDB)	$\delta^{13}C$ (VPDB)	Carbonate Domain	Cement Stratigraphy
−6.76	−3.82	Micrite	Stratum 4
−7.8	−4.43	Micrite	(Stratum 2) U-enriched
−6.54	−3.04	Micrite	Stratum 4
−12.11	−6.22	Sparite	Stratum 4
−7.54	−4.36	Micrite	Stratum 1
−7.54	−4.26	Micrite	Stratum 1
−7.00	−4.06	Micrite	Stratum 1
−7.95	−4.50	Micrite	Stratum 1
−7.14	−4.09	Micrite	Stratum 1
−6.93	−3.66	Micrite	Stratum 1
−6.83	−4.01	Micrite	Stratum 1
−6.90	−3.61	Micrite	Stratum 1
−6.58	−4.21	Micrite	Stratum 1
−8.29	−4.25	Micrite	Stratum 1
−9.58	−5.18	Micrite	Stratum 1
−9.32	−4.12	Micrite	Stratum 1
−4.21	−2.85	Micrite	Stratum 1
−9.65	−4.45	Micrite	Stratum 1
−8.19	−4.28	Micrite	Stratum 1
−5.46	−3.13	Micrite	Stratum 1
−8.43	−4.16	Micrite	Stratum 1
−7.50	−4.83	Micrite	Stratum 1

3.6. Carbonate Clumped Isotope Paleothermometry

A subset of three samples were separately micromilled at SBU from the micrite facies with elevated U based on phosphor imaging (strata 2). These samples were run for carbonate clumped isotopes in the stable isotope laboratory in the SBU Department of Geosciences. The isotope measurements were made using a custom carbonate phosphoric acid digestion and CO_2 purification device (common acid bath at 90 °C) that utilizes cryogenic trapping of water in −80 °C slushes, and CO_2 in liquid nitrogen, coupled to a MAT 253 Plus isotope ratio mass spectrometer [72,73], identical to the one used in [74]. Carbonate carbon, oxygen, and clumped isotopes (denoted by the isotope ratio Δ_{47}) were measured on the micromilled powder. Approximately 6 mg of powdered sample was used for each measurement and two sample measurements were replicated (Table 4).

Table 4. Carbonate clumped isotope measurement results.

Sample	n	$\delta^{13}C \pm 1$ SD	$\delta^{18}O \pm 1$ SD	$\Delta_{47} \pm 1$ SD	T (Δ_{47})	T (Δ_{47})	$\delta^{18}O_{fluid}$	$\delta^{18}O_{fluid}$
		(‰, VPDB)	(‰, VPDB)	(‰, $CDES_{90}$)	(°C)	95% CI *	(‰, VSMOW)	95% CI #
CdrMtn1	1	−3.33	−7.19	0.481	72	12	3.0	1.7
CdrMtn2	2	−4.07 ± 0.04	−8.44 ± 0.06	0.405 ± 0.009	116	12	7.7	1.4
CdrMtn3	3	−4.07 ± 0.03	−8.58 ± 0.05	0.388 ± 0.015	128	13	9.1	1.4

* Clumped isotope temperature 95% confidence intervals (CI) include propagated temperature calibration error (~±3 °C from [71]). A minimum measurement error of ±0.012‰ is assumed for samples where n < 3. # Calculated fluid $\delta^{18}O$ 95% confidence intervals include both T (Δ_{47}) 95% CI and the $\delta^{18}O$ error propagated through the [72] calcite–water oxygen isotope thermometry equation.

The carbonate clumped isotope data were corrected following the established protocols in [75], using standard ^{13}R, ^{17}R, and ^{18}R values from [76]. To calculate micrite clumped isotope temperatures, we used the equation from [77], and to calculate fluid $\delta^{18}O$ values, we used the calcite–water oxygen isotope equation from [78]. The reported error for fluid $\delta^{18}O$ in Table 4 propagates both error in T(Δ_{47}) and carbonate $\delta^{18}O$ measurement through these equations.

4. Results

4.1. Carbonate Petrography

CL imaging analysis and optical microscopy define four carbonate strata in the sample composed of non-luminescent micrite. These strata are bound by zoned and luminescent

microspar and sparite, including common microcrystalline quartz domains (Figure 4). In general, each stratal layer identified is bordered by microcrystalline quartz, and some, but not all, are bordered by cavities infilled with microsparitic cement. The microcrystalline quartz is nonluminescent throughout the entire sample. The first strata contain micrite that is weakly luminescent. Cross-referencing the autoradiography results with the CL analysis indicates that regions of U-enrichment occur in one of the carbonate strata identified as stratum 2 (Figure 4B). Stratum 2 is likewise weakly luminescent to brightly luminescent. Stratum 3 is an irregular domain of micrite that is brightly luminescent everywhere. Stratum 4 is a laminated micrite with alternating bright to dull luminescence. The CL imaging analysis and subsequent identification of microstrata in the sample guided the microsampling protocol for stable isotope analysis.

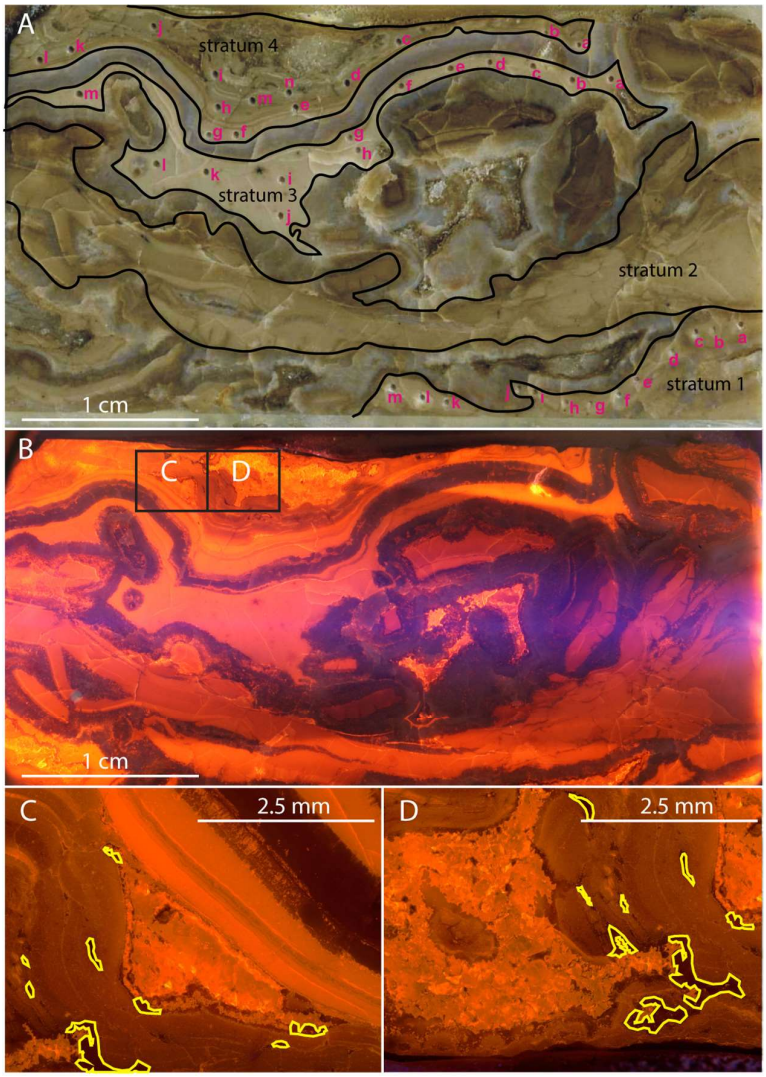

Figure 4. Petrography and cathodoluminescence (CL) results of the studied sample. (**A**) Plain light image of the sample (highlighted in Table 1) and displaying the microsample locations for strata 1 (microsamples a–m), 3, (microsamples a–m) and 4 (microsamples a–n) processed at the University of Kansas for stable isotope analysis. (**B**) CL image of the sample with inset images (**C**,**D**) indicating the location of high-resolution sampling of microsparite in stratum 4. (**C**,**D**) High-resolution sampling areas (yellow) of microsparite in stratum 4 for stable isotope analysis.

4.2. Uranium Chemistry and Spatial Distribution

Element abundance maps produced via LA-ICP-MS reveal a strong spatial relationship between Si and U, in addition to U and Pb existing diffusely within micritic carbonate (Figure 5). Moreover, the carbonate matrix has a surprisingly elevated concentration of Al in the range of 100s of ppm. The REE pattern of the carbonate is very low relative to the post-Archean Australian shale (PAAS). However, Ce is high with a positive Ce anomaly of Ce* = 4.5. The U/Pb of the carbonate matrix outside of the regions indicated by autoradiography is low (average < 2). U-XANES and EXAFS results indicate that U from the micritic carbonate in the sample is tetravalent (Figure 6). XRF maps show that U is the most highly concentrated along micro fractures (Figure 6B). Elevated U concentrations occur within the micrite as diffuse zones of U-enrichment, consistent with the LA-ICP-MS results. RGB maps (U, Fe, Ca) indicate no correlation between U and Fe (Figure 5). This is consistent with the synchrotron XRF results which show anti-correlated regions of the sample with concentrated U versus Fe and Mn.

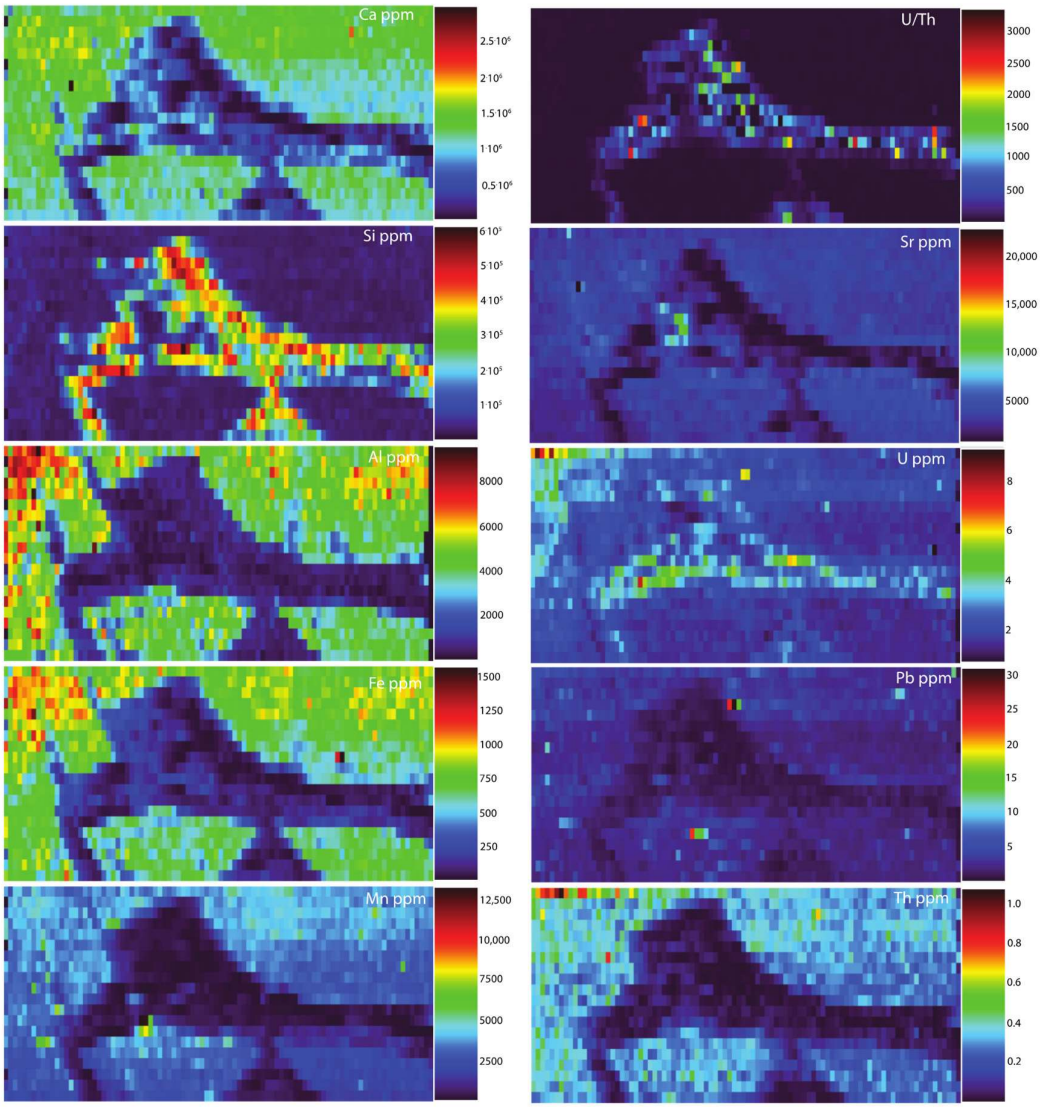

Figure 5. Element distributions in the studied sample via LA. Laser ablation maps of nine elements in the studied sample.

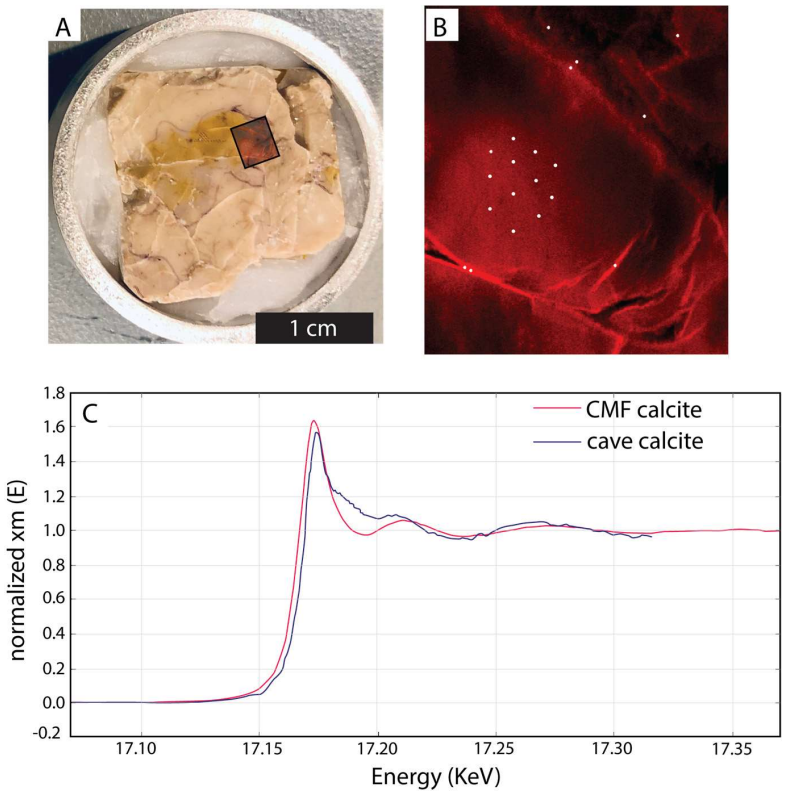

Figure 6. XANES and XRF results of the U-enriched portion of stratum 2. (**A**) Slab of the studied carbonate sample of the Cedar Mountain Formation. The boxed area with the red image is the location of the uranium map in (**B**). (**B**) XRF map of U. The brighter red corresponds to higher U concentrations. Dark areas have lower U concentrations. The white spots are the locations of U-XANES scans. (**C**) Merged U-XANES from the Cedar Mountain Formation carbonate, as well as a cave carbonate with published EXAFS, indicating aligned peaks around 17,153 eV consistent with UO_2.

4.3. Uranium–Lead Geochronology

Two independent LA-ICP-MS campaigns (University of Kansas and SBU) conducted using autoradiography confirmed the locations of radionuclide concentrations in the studied sample. These new LA-ICP-MS results include two new U–Pb ages that are compared to an initial U–Pb age produced by isotope dilution thermal ionization mass spectrometry (ID-TIMS) analysis (Figures 7 and 8). The sub-sampling locations for LA-ICP-MS were determined by autoradiography results of the sample; thus, an identical approach for subsampling carbonate for U and Pb isotopic analysis was performed for ID-TIMS and both LA-ICP-MS campaigns. The original ID-TIMS U–Pb age was based on five spots that were microdrilled from areas of elevated U based on phosphor imaging (Figure 8). The samples analyzed by ID-TIMS gave an age of 119 ± 2.6 Ma. The University of Kansas LA-ICP-MS results indicate an age of 123.66 ± 1.91 Ma (MSWD = 0.53, Figure 7C); whereas the SBU LA-ICP-MS results indicate an overlapping age of 122.3 ± 3.15 Ma (MSWD = 2.0, Figure 7A). The two LA-ICP-MS methods differ principally not in the general data reduction protocol, but rather in the carbonate reference material used. The University of Kansas protocol calibrated the Pb isotope fractionation to NIST614 glass, then the U–Pb age to the DBTL (Duff Brown Tank limestone) reference [79], followed by validation against the WC-1 reference. The calibration protocol at SBU used the NIST612 for the Pb isotope ratio and WC-1 reference material for U–Pb, with an in-house secondary reference material, Barstow. While the LA ages indicate a slightly older age for the sample, the ages all overlap within uncertainty.

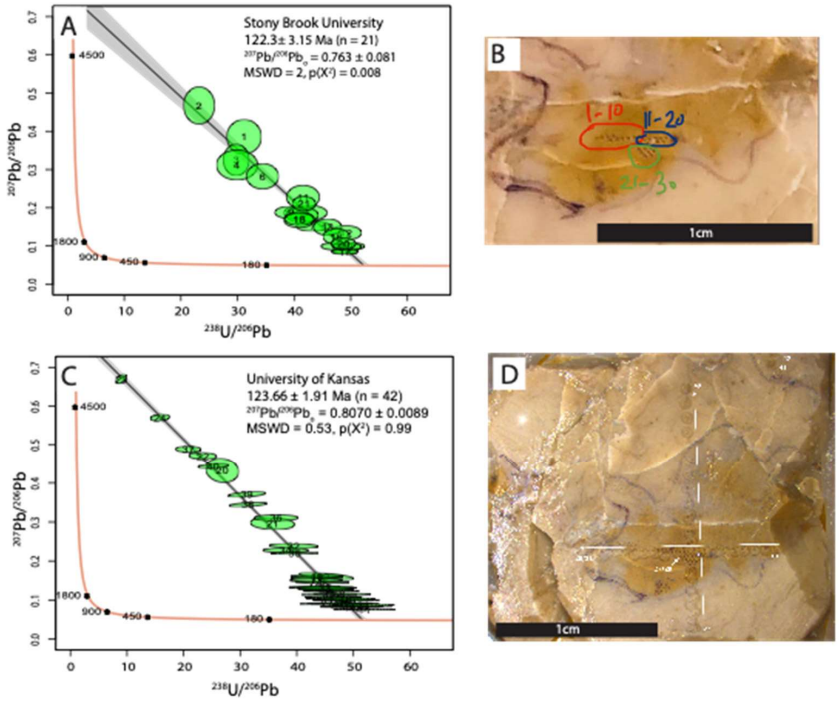

Figure 7. (**A**) Tera–Wasserburg concordia plot of LA-ICP-MS data from Stony Brook University. (**B**) Polished slab with spots for the SBU isochron circled and numbered. The numbers go from left to right and from top to bottom when there are stacked holes. (**C**) Tera–Wasserburg concordia plot of LA-ICP-MS data from the University of Kansas (KU). (**D**) Polished slab with the spots for the KU isochron indicated with arrows and numbers. There is an extra set of spots outside of the region indicated by the arrows from a previous analysis session.

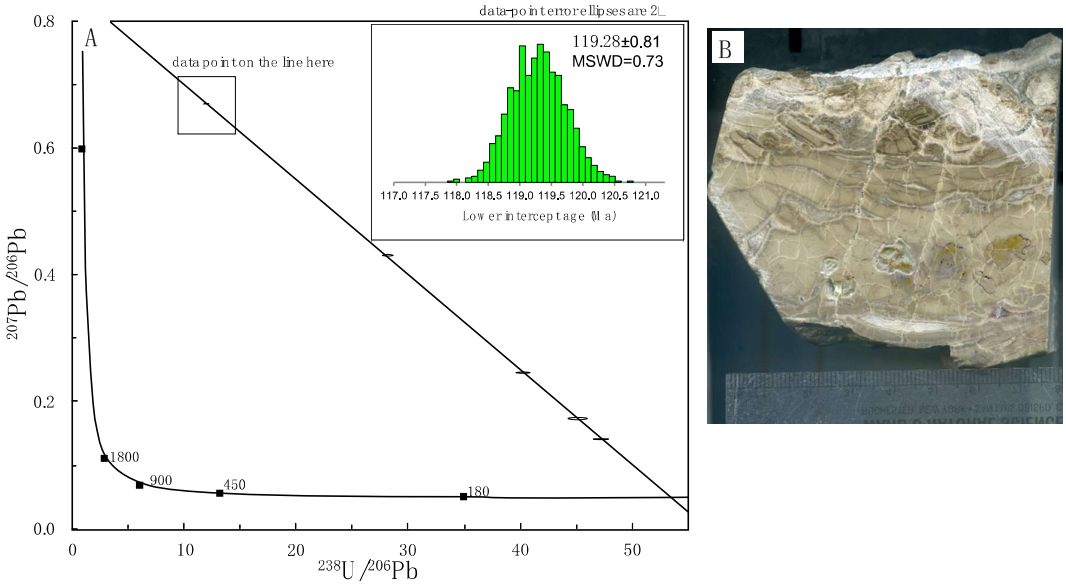

Figure 8. (**A**) Tera–Wasserburg concordia plot of ID-TIMS data. The insert is a histogram of ages based on 1000 Monte Carlo simulations based on the five data points. (**B**) Slab of the Cedar Mountain Formation carbonate that was dated. The micrite in the lower middle part of the sample where there are holes was microdrilled. Two of the sampled areas are on the back of this slab, but along the same horizon. The yellow areas have the highest U concentrations based on phosphor imaging autoradiography.

4.4. Carbon and Oxygen Isotopic Compositions of Carbonate Minerals

Strata 1–3 were sampled at the University of Kansas for $\delta^{18}O$ and $\delta^{13}C$ analysis, whereas strata 2 was sampled at the University of California Davis along with representative samples of microsparite and spar to characterize the isotopic composition of the coarse-grained calcite domains. A summary of the stable isotope results is provided in Table 3. A cross-plot of $\delta^{18}O$ and $\delta^{13}C$ indicates a clustering of the samples that correspond to the zone of U-enrichment in the sample along with the laminated regions of stratum 4 and the non-U-bearing regions of stratum 2 (Figure 9). Strata 1 and 3 correspond to distinctly more negative $\delta^{18}O$ values; however, stratum 4 is unique in that two clusters of data are evident, with the second clustering of data having distinctly more negative $\delta^{18}O$ values than the first cluster, which has a similar isotopic composition to the zone of U-enrichment (Figure 9).

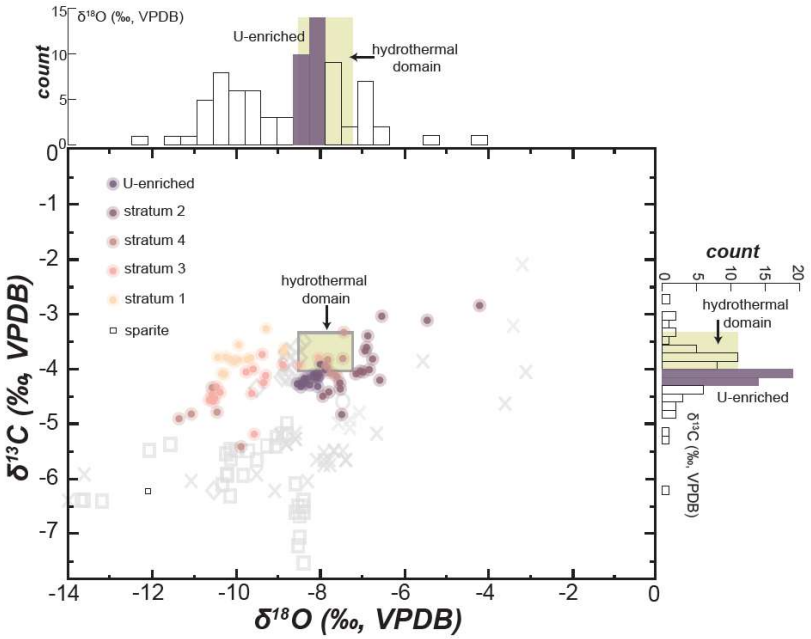

Figure 9. Stable isotope results for the studied palustrine carbonate. The cross plot indicates the $\delta^{18}O$ and $\delta^{13}C$ values of specific strata in the sample. The light gray symbols reflect the summary data from the Cedar Mountain Fm. from Figure 3, for comparison. Sparite from a vug is indicated by the open square symbol. Histograms on the ordinate axis and abscissa highlight the range of $\delta^{18}O$ and $\delta^{13}C$ values of the U-enriched portion of stratum 2 relative to the distribution of all of the strata. The hydrothermal domain is determined from the results of the clumped isotope analysis and reflects an interpretation of the calcite stable O and C isotope results of the clumped isotope analysis.

4.5. Clumped Isotope Paleothermometry

Micrite clumped isotope temperatures from strata 2 (U-bearing micrite) range between 72 and 128 °C (Table 4). The carbon and oxygen isotope values of the clumped isotope sub-samples are generally similar to those from the Yellow Cat member (Figures 3 and 9), and when the measured $\delta^{18}O$ are combined with clumped isotope temperatures, they yield calculated fluid $\delta^{18}O$ values of 3.0 to 9.1‰. Such elevated fluid $\delta^{18}O$ is uncharacteristic for terrestrial and meteoric fluids, and may instead result from micrite crystallization in a rock-buffered system (i.e., low water/rock ratios) or from a carbonate clumped isotope bond reordering during burial heating [80].

5. Discussion

U–Pb geochronology is increasingly applied to terrestrial carbonates in deep-time stratigraphic successions, providing an additional avenue to provide high-precision geochronologic information for stratigraphy [81,82]. The Cedar Mountain Formation sample studied

here provides a unique opportunity to compare ID and LA-ICP-MS carbonate ages. Furthermore, the LA-ICP-MS analyses was performed independently in two separate laboratories, yielding statistically indistinguishable ages that confirm that the U–Pb age recorded by this micritic carbonate is between 116.4–125.57 Ma (Figures 7 and 8). These ages, based on the geochemical and petrographic observations of U-incorporation into the micrite of these samples and the clumped isotope temperatures, are interpreted as maximum depositional ages for the overall carbonate sample as the U-incorporation and U–Pb ages likely reflect early diagenesis. Thus, if authigenic stable isotope compositions are preserved in this sample, then those carbonate components likely predate the timing of U-incorporation in the micritic components of the studied sample.

The method of incorporation of U into the sample has direct implications for interpreting the U–Pb age. One possible mechanism for U incorporation is through direct substitution of U^{4+} for Ca^{2+} [83,84], or via coordinated complexation of $UO_2{}^{2+}$ with Ca and CO_3 [85]. The oxidation state of uranyl-U in this sample is determined to be tetravalent via XANES (Figure 6). Thus, U incorporation into the micrite of stratum 2 is most likely through direct substitution of U^{4+} for Ca^{2+}, similar to results from a Mississippi Valley-type calcite studied by [84]. The elevated Ce anomaly detected in this micrite phase (stratum 2) also indicates a prevalence for water–rock interaction of this carbonate mineral in an overall reducing environment. In addition, the CL imaging results further indicate that the U-enriched micrite has slightly elevated concentrations of Mn and/or Fe^{2+} (Figure 4). Thus, the prevalence of redox-sensitive element abundances in the micrite and the IV oxidation state of U indicate that a reducing fluid interacted with or was the parent fluid for this micrite.

The clumped isotope temperatures of ~75–125 °C indicate that this carbonate (re)precipitation occurred in one of three possible subsurface environments: (1) during moderate to deep burial (~2–4 km assuming a generic 25 °C/km geothermal gradient) [86]; (2) hydrothermal alteration during burial [87,88]; or (3) hydrothermal alteration at or near the time of carbonate sediment accumulation. Bond reordering during burial heating [89,90] is also a probable mechanism to explain the elevated clumped isotope temperatures. However, the association of U with microfractures and Si concentrations in the studied sample, the tetravalent nature of U in the sample, and the general low Eh environment recorded by Fe, Mn, and Ce in the U-bearing micrite indicate that fluid–rock interaction (albeit in a rock-buffered system) describes a family of scenarios most consistent with the data presented herein. The U–Pb age information of these carbonate components adds crucial context [91] to eliminate a burial diagenesis environment as the mechanism/timing of U-incorporation, as strata underlying the studied sample in the Yellow Cat member produce an age of 136 ± 1.3 Ma [21], with an additional age of ca. 131 Ma ~3 m below this sample at the study location [31]. However, the potential effects of Pb-loss on the zircon crystals producing these ages, and over-dispersion of ages [92], mean that these ages may well reflect overly young age estimates for Yellow Cat member strata. Thus, unreasonably low depositional rates would have to be invoked to explain the age disparity of the studied sample with the maximum depositional ages of the underlying paleosols. Moreover, there are no disconformable/nonconformable contacts between the Yellow Cat member and the overlying Ruby Ranch and Mussentuchit members that would indicate burial and exhumation of the studied strata prior to the deposition of volcaniclastic material in the Mussentuchit member, which produces ages of ca. 97 Ma, approximately 100 m higher than the studied sample. Therefore, it is not plausible to achieve both the age of the carbonate domain with elevated temperatures and a burial depth of 2–4 km. However, given the short vertical distance between the Yellow Cat member U–Pb deposition age of 136 ± 1.3 Ma and the sample studied herein that produces an age between 119–123 Ma, it seems likely that the U–Pb reported for this calcite material reflects immobilization and incorporation of U into calcite during early diagenesis/shallow burial. However, deeper burial depths are consistent with other diagenetic domains in carbonate material of the Cedar Mountain Formation. Robertson et al. [40] report intergranular volumes filled with

poikilotopic calcite cements, consistent with a burial depth of 2–3 km [86], with further evidence for fluid–rock interaction and oxygen isotope exchange reactions in these via large variance in, and very negative values of, $\delta^{18}O$ values (Figure 3). These results indicate hydrothermal fluid–rock interaction at great depth. However, the $\delta^{18}O$ values of the carbonate domains (Figure 9) and estimated $\delta^{18}O$ values of the interacting fluid do not display the same range of values as indicated in [40], indicating a different location/timing of the fluid–rock interaction in these U-enriched carbonate domains. Therefore, the most likely scenario to explain the U–Pb ages, redox poise of the U-emplacing fluid, and the elevated clumped isotope temperatures is supergene hydrothermal interaction. Geologic evidence supporting this interpretation includes the presence of vertical to subvertical tufa extending from the Upper Jurassic strata and terminating in the Lower Cretaceous Cedar Mountain Formation in north-western Colorado. The termination of this tufa is in a laterally continuous and bedded radially fibrous calcite (outcrops near Deerlodge Campground, 40.43851 N, 108.52409 W). The existence of these tufa columns indicates an active hydrothermal system in the study region during the Early Cretaceous, which adds support to the interpretation that hydrothermal fluids interacted with sediments at shallow depths, and therefore soon after deposition.

The studied sample exhibits a complex association of carbonate and quartz cements in addition to brecciation of the carbonate matrix. Interpretations of the authigenic formation of the carbonate are based on: (1) the prevalence of micrite; (2) microfractures consistent with contraction of the micrite volume; and (3) the laminar nature of micrite (Figure 4A). These features are consistent with a palustrine-type carbonate [93–95], which exhibits both bedded carbonate during lacustrine conditions and aspects of pedogenic carbonate in the form of brecciation and desiccation. The luminescent microsparite and quartz cements are interpreted to have formed during diagenesis, containing high concentrations of dissolved silica and low dissolved oxygen concentrations. The near complete envelopment of micritic laminae by these cements attests to the unusually high porosity of this material during fluid migration through the sample. Moreover, the elevated Al-concentrations of this carbonate (Figure 5) is consistent with the residual accumulation of Al in the pedogenic environment [96]. The occurrence of elevated U in just one of the micritic laminae indicates U emplacement close to the time of deposition. Conversely, if U was incorporated during later stage diagenesis, it would be expected to correlate with petrographically and CL-identified diagenetic domains in the sample and perhaps would be more ubiquitous (cf. Figure 6B). Autoradiography indicates heterogenous U distributions at the hand sample scale, whereas XRF and LA maps of U-enriched zones confirm that U emplacement in the micrite is homogenous at the domain scale. These results are consistent with XRF microprobe maps of U concentrations in other calcite samples that contain U(IV) that has become part of the substituted calcite lattice [84], rather than an incorporation of uraniferous minerals or inclusions of organo-metal complexes. Moreover, the enhanced U concentrations along microfractures and the surfaces of micrite bordered by quartz cements indicates the possible effects from calcite dissolution of U-substituted calcite. This correlation with fractures may also be consistent with a hydrothermal emplacement mechanism of U in this sample. Zhang et al. [97] reported enhanced dissolution of calcite with high U concentrations, which was followed by precipitation of U-concentrated secondary minerals on surfaces. If such a situation explains the discrepancy between diffuse U concentrations in the micrite strata versus high U concentrations along microfractures and lamina surfaces, then this provides evidence for the relative dating of U incorporation prior to the emplacement of the prominent later stage diagenetic components of the sample.

An alternate hypothesis for U incorporation into this calcite is developed based on the elevated U concentrations of quartz cements in the sample. In this scenario, U migration would accompany the fluids that precipitated these cements, and water–rock interaction with the micrite would lead to substitution of tetravalent U in the calcite lattice under locally reducing conditions. Thus, if the U emplacement in the micritic stratum 2 lamina was derived from diffusion or reaction with a later stage fluid that precipitated the quartz or

microsparite cements, it would be expected that re-equilibration (especially of $\delta^{18}O$ values) to these fluids would ocrur. However, the elevated calculated $\delta^{18}O$ values of the fluid required by the clumped isotope temperatures indicate a rock-buffered fluid interaction scenario; thus, alteration of the authigenic $\delta^{18}O$ values for the studied carbonate component was likely of a lower magnitude than the later stage alteration described in [40]. Stratum 4, however, while not U-bearing, displays an anticipated isotopic trend of re-equilibration in the form of two distinct clusters of $\delta^{18}O$ and $\delta^{13}C$ values, indicating that this carbonate lamina underwent isotopic exchange at some later stage relative to the timing of authigenic carbonate precipitation. Thus, this alternate hypothesis is not supported by the range of geochemical observations tied to the petrography of this sample.

The implications of the U–Pb ages reported here primarily concern the correlation of stable isotope results in a chemostratigraphic context. The U–Pb ages are interpreted to reflect the incorporation of U during early stages of diagenesis of this material, likely in the subsurface, and in a reducing environment. Thus, stable isotope data interpreted to be authigenic from these micritic carbonate domains [18,19] likely formed earlier than the emplacement of U and most likely represent an older phase of carbonate precipitation than the U–Pb ages between 119–123 Ma described herein. Even if the carbonates underwent burial diagenesis, the clumped isotope results indicate that this was under low water–rock ratio conditions; $\delta^{13}C$ is known to be conservative when carbonate diagenesis is rock-buffered [98,99], and this may partially (or completely) explain the observed variability in Yellow Cat (this study) and Poison Strip member $\delta^{18}O$ values [40]. The LA-ICP-MS ages of 122.3 $\pm$ 3.15 Ma and 123.66 $\pm$ 1.91 Ma likely define the time interval in which the studied strata experienced: (1) hydrothermal fluid interaction; (2) clumped isotope resetting from this hydrothermal fluid interaction; (3) and immobilization and incorporation of U into a carbonate phase within the studied strata; all of which postdate the timing of any authigenic stable isotope ratios preserved in these strata and provide a maximum stratigraphic age for this sample. Furthermore, the lower members of the Cedar Mountain Formation are now bracketed by two different geochronometers: (1) zircon crystal U–Pb ages; and (2) calcite U–Pb ages. The implications for the application of these two geochronometers to the same strata is that interpretations of zircon crystallization ages indicate that the strata containing the zircons must be as old or younger than the zircon crystal U–Pb age; conversely, the U–Pb carbonate ages indicate that the strata is as old or older than the carbonate U–Pb age. Therefore, these two geochronometers provide important brackets on depositional versus diagenetic events that affect the strata under investigation.

The implications of the new U–Pb ages and U chemistry of the studied sample indicate that stable isotopic data interpreted to reflect authigenic paleoenvironmental/paleoclimatic conditions (Figure 9) likely pre-date the U–Pb age ranges quoted herein (Figures 7 and 8). The Early Cretaceous stages of Valanginian–Barremian are plausible time intervals in which the authigenic stable isotope values were fixed in the studied sample. Below, the paleoclimate trends for these Early Cretaceous stages are summarized to assess which stage most likely corresponds to the chemostratigraphic record preserved in this stratigraphic interval. The Valanginian records a prominent decline in paleoatmospheric CO_2 concentrations and global cooling that overlap in age with the Paraná-Etendeka LIP [29]. If the stratigraphic trends in terrestrial $\delta^{13}C$ (Figure 2) can be expected to correlate with the marine chemostratigraphy, then it is unlikely the studied sample falls within this interval due to the pronounced negative isotope excursion preserved in the stratigraphic interval that the sample was collected from. The Hauterivian of the Canadian Arctic records yet another LIP-influenced paleoclimate interval. However, the climate archive of this paleo high-latitude setting indicates a cool–warm–cool paleoclimate fluctuation throughout the Hauterivian [100]. A contemporaneous low paleolatitude setting in the Sichuan Basin, reflecting a fully terrestrial depositional environment, records cool and arid conditions during the middle Valanginian, but with a marked increase in temperature and an increase in the ratio of precipitation/evapotranspiration by the late Valanginian/early Hauterivian [101]. The Hauterivian–Barremian, at a similar paleolatitude to the studied depositional

basin, the North Sea borderlands, record high frequency (precession-scale) fluctuations in inferred aridity and humidity [102]. The Valanginian–Hauterivian paleoclimate record from the Canadian Arctic and Sichuan Basin display promising "event"-like changes in paleoclimate that are consistent with the positive excursion in $\delta^{13}C$ recorded in the stratigraphic interval studied herein. Moreover, these climate trends are associated with the High Arctic LIP, which presents one mechanism that can plausibly explain global climate change, which can also explain a positive carbon isotope excursion through the invasion of mantle-derived carbon to the atmospheric reservoir. Thus, while previous data from the studied sample have been interpreted to correlate with the OAE-1a ("Selli Event"), the U–Pb ages and clumped isotope thermometry here indicate that the authigenic stable isotope values recorded in the Yellow Cat member most parsimoniously overlap in time with the Valanginian–Hauterivian, which was likewise a time of global climate change, possibly induced or modulated by LIP volcanism.

6. Conclusions

The geochronology and geochemistry of uranium emplacement in a terrestrial carbonate is studied via petrography and a range of geochemical and spectroscopic methods. LA ICP-MS results for U–Pb geochronology provide two new ages of 122.3 ± 3.15 Ma and 123.66 ± 1.91 Ma Ma based on analysis in two independent laboratories. High-resolution element maps of the studied samples indicate that U emplacement occurred in two distinct regions: (1) in a micritic carbonate lamina; and (2) within diagenetic quartz cements and micro fractures within the micritic lamina. U-XANES data indicate that the U is tetravalent. Reducing conditions likely explain the incorporation of U into the micritic calcite, as evidenced by the prevalence of redox sensitive elements and a positive Ce anomaly. Spatial heterogeneity of U concentrations is consistent with an early diagenetic incorporation of U, followed by subsequent fluid–rock interactions, whose conditions are constrained by elevated carbonate clumped isotope temperatures, and the development of distinctly elevated U concentrations along micro fractures and microcrystalline quartz cements. These results indicate that the U–Pb ages reported herein most likely reflect an early diagenetic event in the subsurface, and that the uncertainties about the range of isotopic ages likely constrains the timing of authigenic carbonate stable isotope values, particularly $\delta^{13}C$, in the micritic components of this complex sample prior to the U–Pb age information.

Supplementary Materials: The following supporting information can be downloaded at: https://www.mdpi.com/article/10.3390/geosciences12090346/s1, Table S1: Stable C and O isotope compilation of pedogenic calcite in the Cedar Mountain Formation; Table S2: Isotope Dilution data for U-Pb; Table S3: Laser Ablation data from Stony Brook University; Table S4: Laser Ablation data from the University of Kansas.

Author Contributions: Conceptualization, E.L.G., E.T.R., G.A.L. and J.A.M.; Formal analysis, E.L.G., E.T.R., G.A.L., A.M., G.A.H., P.N. and R.S.S.; Methodology, G.A.L., A.M., R.V.T. and K.M.W.; Project administration, E.L.G.; Validation, E.T.R., G.A.L., A.M. and G.A.H.; Writing—original draft, E.L.G., E.T.R. and G.A.L.; Writing—review & editing, E.T.R., G.A.L., A.M., G.A.H., M.B.S. and P.N. All authors have read and agreed to the published version of the manuscript.

Funding: This research received no external funding.

Conflicts of Interest: The authors declare no conflict of interest.

References

1. Schlanger, S.O.; Jenkyns, H.C. Cretaceous oceanic anoxic events: Causes and consequences. *Geol. Mijnb.* **1976**, *55*, 179–184.
2. Scholle, P.A.; Arthur, M.A. Carbon isotope fluctuations in Cretaceous pelagic limestones: Potential stratigraphic and petroleum exploration tool. *Am. Assoc. Pet. Geol. Bull.* **1980**, *64*, 67–87.
3. Jarvis, I.; Gale, A.; Jenkyns, H.C.; Pearce, M.A. Secular variation in Late Cretaceous carbon isotopes: A new $\delta^{13}C$ carbonate reference curve for the Cenomanian-Campanian (99.6–70.6 Ma). *Geol. Mag.* **2006**, *143*, 561–608. [CrossRef]
4. Jenkyns, H.C. Geochemistry of oceanic anoxic events. *Geochem. Geophys. Geosyst.* **2010**, *11*. [CrossRef]

5. Zhang, X.; Chen, K.; Hu, D.; Sha, J. Mid-Cretaceous carbon cycle perturbations and Oceanic Anoxic Events recorded in southern Tibet. *Sci. Rep.* **2016**, *6*, 39643. [CrossRef] [PubMed]
6. Leckie, R.M.; Bralower, T.J.; Cashman, R. Oceanic anoxic events and plankton evolution: Biotic response to tectonic forcing during the mid-Cretaceous. *Paleoceanography* **2002**, *17*, 13-1–13-29. [CrossRef]
7. Taylor, B. The single largest oceanic plateau: Ontong Java–Manihiki–Hikurangi. *Earth Planet. Sci. Lett.* **2006**, *241*, 372–380. [CrossRef]
8. Erba, E.; Duncan, R.A.; Bottini, C.; Tiraboschi, D.; Weissert, H.; Jenkyns, H.C.; Malinverno, A. Environmental consequences of Ontong Java Plateau and Kerguelen Plateau volcanism. In *The Origin, Evolution, and Environmental Impact of Oceanic Large Igneous Provinces*; Geological Society of America: Boulder, CO, USA, 2015; Volume 511, pp. 271–303. [CrossRef]
9. Malinverno, A.; Erba, E.; Herbert, T.D. Orbital tuning as an inverse problem: Chronology of the early Aptian oceanic anoxic event 1a (Selli Level) in the Cismon APTICORE. *Paleoceanography* **2010**, *25*. [CrossRef]
10. Malinverno, A.; Hildebrandt, J.; Tominaga, M.; Channell, J.E.T. M-sequence geomagnetic polarity time scale (MHTC12) that steadies global spreading rates and incorporates astrochronology constraints. *J. Geophys. Res. Earth Surf.* **2012**, *117*. [CrossRef]
11. Hasegawa, T. Cenomanian-Turonian carbon isotope events recorded in terrestrial organic matter from northern Japan. *Palaeogeogr. Palaeoclim. Palaeoecol.* **1997**, *130*, 251–273. [CrossRef]
12. Gröcke, D.; Hesselbo, S.P.; Jenkyns, H. Carbon-isotope composition of Lower Cretaceous fossil wood: Ocean-atmosphere chemistry and relation to sea-level change. *Geology* **1999**, *27*, 155–158. [CrossRef]
13. Gröcke, D.R.; Price, G.D.; Robinson, S.A.; Baraboshkin, E.Y.; Mutterlose, J.; Ruffell, A.H. The upper Valangian (Early Cretaceous) positive carbon-isotope event recorded in terrestrial plants. *Earth Planet. Sci. Lett.* **2005**, *240*, 495–509. [CrossRef]
14. Gröcke, D.; Ludvigson, G.A.; Witzke, B.L.; Robinson, S.; Joeckel, R.M.; Ufnar, D.F.; Ravn, R.L. Recognizing the Albian-Cenomanian (OAE1d) sequence boundary using plant carbon isotopes: Dakota Formation, Western Interior Basin, USA. *Geology* **2006**, *34*, 193–196. [CrossRef]
15. Ando, A.; Kakegawa, T. Carbon isotope records of terrestrial organic matter and the occurrence of planktonic foraminifera from the Albian stage of Hokkaido, Japan: Ocean-atmosphere $\delta^{13}C$ trends and chronostratigraphic implications. *Palaios* **2007**, *22*, 417–432. [CrossRef]
16. Jahren, A.H.; Arens, N.C.; Sarmiento, G.; Guerrero, J.; Amundson, R. Terrestrial record of methane hydrate dissociation in the Early Cretaceous. *Geology* **2001**, *29*, 159–162. [CrossRef]
17. Jacobs, L.L.; Ferguson, K.; Polcyn, M.J.; Rennison, C. Cretaceous $\delta^{13}C$ stratigraphy and the age dinosaurs and early mosasaurs. *Geol. Mijnb.* **2005**, *84*, 257–268. [CrossRef]
18. Ludvigson, G.A.; Joeckel, R.M.; Gonzalez, L.; Gulbranson, E.L.; Rasbury, T.; Hunt, G.J.; Kirkland, J.I.; Madsen, S. Correlation of Aptian-Albian Carbon Isotope Excursions in Continental Strata of the Cretaceous Foreland Basin, Eastern Utah, U.S.A. *J. Sediment. Res.* **2010**, *80*, 955–974. [CrossRef]
19. Ludvigson, G.; Joeckel, R.; Murphy, L.; Stockli, D.; González, L.; Suarez, C.; Kirkland, J.; Al-Suwaidi, A. The emerging terrestrial record of Aptian-Albian global change. *Cretac. Res.* **2015**, *56*, 1–24. [CrossRef]
20. Li, X.; Xu, W.; Liu, W.; Zhou, Y.; Wang, Y.; Sun, Y.; Liu, L. Climatic and environmental indications of carbon and oxygen isotopes from the Lower Cretaceous calcrete and lacustrine carbonates in Southeast and Northwest China. *Palaeogeogr. Palaeoclimatol. Palaeoecol.* **2013**, *385*, 171–189. [CrossRef]
21. Joeckel, R.M.; Ludvigson, G.A.; Möller, A.; Hotton, C.L.; Suarez, M.B.; Suarez, C.A.; Sames, B.; Kirkland, J.I.; Hendrix, B. Chronostratigraphy and terrestrial palaeoclimatology of Berriasian–Hauterivian strata of the Cedar Mountain Formation, Utah, USA. *Geol. Soc. Lond. Spec. Publ.* **2019**, *498*, 75–100. [CrossRef]
22. Suarez, M.B.; Knight, J.A.; Godet, A.; Ludvigson, G.A.; Snell, K.E.; Murphy, L.; Kirkland, J.I. Multiproxy strategy for determining palaeoclimate parameters in the Ruby Ranch Member of the Cedar Mountain Formation. *Geol. Soc. Lond. Spec. Publ.* **2020**, *507*, 313–334. [CrossRef]
23. Kirkland, J.; Suarez, M.; Suarez, C.; Hunt-Foster, R. The Lower Cretaceous in east-central Utah—The Cedar Mountain Formation and its bounding strata. *Geol. Intermt. West* **2016**, *3*, 101–228. [CrossRef]
24. Kirkland, J.I.; Burge, D.; Gaston, R. Lower to Middle Cretaceous dinosaur faunas of the central Colorado Plateau: A key to understanding 35 million years of tectonics, sedimentology, evolution, and biogeography. *Brigh. Young Univ. Geol. Stud.* **1997**, *42*, 69–104.
25. Kirkland, J.I.; Madsen, S.K. The Lower Cretaceous Cedar Mountain Formation, eastern Utah–the view up an always interesting learning curve. In *Field Guide to Geological Excursions in Southern Utah, Proceedings of the Geological Society of America Rocky Mountain Section 2007 Annual Meeting, Grand Junction Geological Society and Utah Geological Association Publication, St. George, UT, USA, 4–6 May 2007*; Lund, W.R., Ed.; Utah Geological Association: Salt Lake City, UT, USA, 2007; Volume 35, pp. 1–108.
26. Lawton, T.F.; Hunt, G.J.; Gehrels, G.E. Detrital zircon record of thrust belt unroofing in Lower Cretaceous synorogenic conglomerates, central Utah. *Geology* **2010**, *38*, 463–466. [CrossRef]
27. Hunt, G.J.; Lawton, T.F.; Kirkland, J.I. Detrital zircon U-Pb geochronological provenance of Lower Cretaceous strata, foreland basin, Utah. In *Sevier Thrust Belt: Northern and Central Utah and Adjacent Areas. Utah Geological Association Publication*; Sprinkel, D.A., Yonkee, W.A., Chidsey, T.C., Jr., Eds.; Utah Geological Association Publication: Salt Lake City, UT, USA, 2011; Volume 40, pp. 193–211.

28. Mattioli, E.; Pittet, B.; Riquier, L.; Grossi, V. The mid-Valanginian Weissert Event as recorded by calcareous nannoplankton in the Vocontian Basin. *Palaeogeogr. Palaeoclim. Palaeoecol.* **2014**, *414*, 472–485. [CrossRef]
29. Cavalheiro, L.; Wagner, T.; Steinig, S.; Bottini, C.; Dummann, W.; Esegbue, O.; Gambacorta, G.; Giraldo-Gómez, V.; Farnsworth, A.; Flögel, S.; et al. Impact of global cooling on Early Cretaceous high pCO_2 world during the Weissert Event. *Nat. Commun.* **2021**, *12*, 5411. [CrossRef] [PubMed]
30. Cifelli, R.L.; Kirkland, J.I.; Weil, A.; Deino, A.L.; Kowallis, B.J. High-precision $^{40}Ar/^{39}Ar$ geochronology and the advent of North America's Late Cretaceous terrestrial fauna. *Proc. Natl. Acad. Sci. USA* **1997**, *94*, 11163–11167. [CrossRef] [PubMed]
31. Joeckel, R.M.; Suarez, C.A.; McLean, N.M.; Möller, A.; Ludvigson, G.A.; Suarez, M.B.; Kirkland, J.I.; Kiessling, S.; Hatzell, G. First Identification in Terrestrial Sediments and In-Situ Radiometric Dating of Valanginian Weissert Event; Yellow Cat Member, Cedar Mountain Formation, Eastern Utah, USA. *Geosciences*, 2022; *in press*.
32. Garrison, J.R., Jr.; Brinkman, D.; Nichols, D.J.; Layer, P.; Burge, D.; Thayn, D. A multidisciplinary study of the Lower Cretaceous Cedar Mountain Formation, Mussentuchit Wash, Utah: A determination of the paleoenvironment and paleoecology of the Eolambia caroljonesa dinosaur quarry. *Cretac. Res.* **2007**, *28*, 461–494. [CrossRef]
33. Tucker, R.T.; Zanno, L.E.; Huang, H.-Q.; Makovicky, P.J. A refined temporal framework for newly discovered fossil assemblages of the upper Cedar Mountain Formation (Mussentuchit Member), Mussentuchit Wash, Central Utah. *Cretac. Res.* **2020**, *110*, 104384. [CrossRef]
34. Moorbath, S.; Taylor, P.N.; Orpen, J.L.; Treloar, P.; Wilson, J.F. First direct radiometric dating of Archaean stromatolitic limestone. *Nature* **1987**, *326*, 865–867. [CrossRef]
35. Smith, P.E.; Farquhar, R.M. Direct dating of Phanerozoic sediments by the ^{238}U–^{206}Pb method. *Nature* **1989**, *341*, 518–521. [CrossRef]
36. Rasbury, E.T.; Cole, J.M. Directly dating geologic events: U-Pb dating of carbonates. *Rev. Geophys.* **2009**, *47*. [CrossRef]
37. Shapiro, R.S.; Fricke, H.C.; Fox, K. Dinosaur-bearing oncoids from ephemeral lakes of the Lower Cretaceous Cedar Mountain Formation, Utah. *PALAIOS* **2009**, *24*, 51–58. [CrossRef]
38. Suarez, C.A.; González, L.A.; Ludvigson, G.A.; Cifelli, R.L.; Tremain, E. Water utilization of the Cretaceous Mussentuchit Member local vertebrate fauna, Cedar Mountain Formation, Utah, USA: Using oxygen isotopic composition of phosphate. *Palaeogeogr. Palaeoclim. Palaeoecol.* **2012**, *313–314*, 78–92. [CrossRef]
39. Suarez, C.A.; Gonzalez, L.A.; Ludvigson, G.A.; Kirkland, J.I.; Cifelli, R.L.; Kohn, M.J. Multi-Taxa Isotopic Investigation of Paleohydrology in the Lower Cretaceous Cedar Mountain Formation, Eastern Utah, U.S.A.: Deciphering Effects of the Nevadaplano Plateau on Regional Climate. *J. Sediment. Res.* **2014**, *84*, 975–987. [CrossRef]
40. Robertson, C.; Ludvigson, G.A.; Joeckel, R.; Mohammadi, S.; Kirkland, J.I. Differentiating early from later diagenesis in a Cretaceous sandstone and petroleum reservoir of the Cedar Mountain Formation, Utah. *Rocky Mt. Geol.* **2021**, *56*, 19–36. [CrossRef]
41. Arens, N.C.; Harris, E.B. Paleoclimatic reconstruction for the Albian–Cenomanian transition based on a dominantly angiosperm flora from the Cedar Mountain Formation, Utah, USA. *Cretac. Res.* **2015**, *53*, 140–152. [CrossRef]
42. Harris, E.B.; Arens, N.C. A mid-Cretaceous angiosperm-dominated macroflora from the Cedar Mountain Formation of Utah, USA. *J. Paleontol.* **2016**, *90*, 640–662. [CrossRef]
43. Lohmann, K.C. Geochemical patterns of meteoric diagenetic systems and their application to studies of paleokarst. In *Paleokarst*; James, N.P., Choquette, P.W., Eds.; Springer: New York, NY, USA, 1988; pp. 58–80.
44. Kirkland, J.I.; Zanno, L.E.; Sampson, S.D.; Clark, J.M.; DeBlieux, D.D. A primitive therizinosaurid dinosaur from the Early Cretaceous of Utah. *Nature* **2005**, *435*, 84–87. [CrossRef]
45. Currie, B.S. Structural configuration of the Early Cretaceous cordilleran foreland-basin system and Sevier thrust belt, Utah and Colorado. *J. Geol.* **2002**, *110*, 697–718. [CrossRef]
46. Ufnar, D.; González, L.; Ludvigson, G.; Brenner, R.; Witzke, B. Evidence for increased latent heat transport during the Cretaceous (Albian) greenhouse warming. *Geology* **2004**, *32*, 1049–1052. [CrossRef]
47. Suarez, M.B.; González, L.A.; Ludvigson, G.A.; Vega, F.J.; Alvarado-Ortega, J. Isotopic composition of low-latitude paleoprecipitation during the Early Cretaceous. *GSA Bull.* **2009**, *121*, 1584–1595. [CrossRef]
48. Heller, P.L.; Paola, C. The paradox of Lower Cretaceous gravels and the initiation of thrusting in the Sevier orogenic belt, United States Western Interior. *GSA Bull.* **1989**, *101*, 864–875. [CrossRef]
49. Yingling, V.L.; Heller, P.L. Timing and record of foreland sedimentation during the initiation of the Sevier orogenic belt in central Utah. *Basin Res.* **1992**, *4*, 279–290. [CrossRef]
50. Miall, A.D. Reservoir Heterogeneities in Fluvial Sandstones: Lessons from Outcrop Studies. *AAPG Bull.* **1988**, *72*, 682–697. [CrossRef]
51. DeCelles, P.G. Sedimentation in a tectonically partitioned, nonmarine foreland basin: The Lower Cretaceous Kootenai Formation, southwestern Montana. *GSA Bull.* **1986**, *97*, 911–931. [CrossRef]
52. Britt, B.B.; Scheetz, R.D.; Brinkman, D.B.; Eberth, D.A. A Barremian neochoristodere from the Cedar Mountain Formation, Utah, U.S.A. *J. Vertebr. Paleontol.* **2006**, *26*, 1005–1008. [CrossRef]
53. Aubrey, W.M. A newly discovered, widespread fluvial facies and unconformity marking the Upper Jurassic/Lower Cretaceous boundary, Colorado Plateau. In The Upper Jurassic Morrison Formation—An Interdisciplinary Study, Part I: Modern Geology; Carpenter, K., Chure, D., Kirkland, J.I., Eds.; 1998; Volume 22, pp. 209–233.

54. Demko, T.M.; Currie, B.S.; Nicoll, K.A. Regional paleoclimatic and stratigraphic implications of paleosols and fluvial/overbank architecture in the Morrison Formation (Upper Jurassic), Western Interior, USA. *Sediment. Geol.* **2004**, *167*, 115–135. [CrossRef]
55. Myers, T.S.; Tabor, N.J.; Rosenau, N.A. Multiproxy approach reveals evidence of highly variable paleoprecipitation in the Upper Jurassic Morrison Formation (western United States). *GSA Bull.* **2014**, *126*, 1105–1116. [CrossRef]
56. Jordan, T.E. Thrust Loads and Foreland Basin Evolution, Cretaceous, Western United States. *AAPG Bull.* **1981**, *65*, 2506–2520. [CrossRef]
57. DeCelles, P.G.; Coogan, J.C. Regional structure and kinematic history of the Sevier fold-thrust belt, central Utah: Implications for the Cordilleran magmatic arc and foreland basin system. *GSA Bull.* **2006**, *118*, 841–864. [CrossRef]
58. Dickinson, W.R.; Gehrels, G.E. Sediment delivery to the Cordilleran foreland basin: Insights from U-Pg ages of detrital zircons in Upper Jurassic and Cretaceous strata of the Colorado Plateau. *Am. J. Sci.* **2008**, *308*, 1041–1082.
59. Suarez, M.; Suarez, C.; Al-Suwaidi, A.; Hatzell, G.; Kirkland, J.; Salazar-Verdin, J.; Ludvigson, G.; Joeckel, R. Terrestrial Carbon Isotope Chemostratigraphy in the Yellow Cat Member of the Cedar Mountain Formation. In *Terrestrial Depositional Systems*; Elsevier: Amsterdam, The Netherlands, 2017; pp. 303–336. [CrossRef]
60. Al-Suwaidi, A.H. A Ped's Story–Weathering out Climatic Change during the Mid-Cretaceous. Master's Thesis, University of Kansas, Lawrence, KS, USA, 2007; 134p.
61. Kirschbaum, M.A.; Schenk, C.J. *Sedimentology and Reservoir Heterogeneity of a Valley-Fill Deposit—A Field Guide to the Dakota Sandstone of the San Rafael Swell, Utah*; US Geological Survey: Reston, VA, USA, 2011. [CrossRef]
62. Montgomery, E. Limnogeology and Chemostratigraphy of Carbonates and Organic Carbon from the Cedar Mountain Formation (CMF), Eastern Utah. Master's Thesis, University of Texas San Antonio, San Antonio, TX, USA, 2014; 68p.
63. Sprinkel, D.A.; Madsen, S.K.; Kirkland, J.I.; Waanders, G.L.; Hunt, G.J. Cedar Mountain and Dakota Formations around Dinosaur National Monument–evidence of the first incursion of the Cretaceous Western Interior Seaway into Utah. In *Utah Geological Survey Special Study*; Utah Geological Survey: Salt Lake City, UT, USA, 2012; Volume 143, 21p.
64. Cole, J.M.; Nienstedt, J.; Spataro, G.; Rasbury, E.T.; Lanzirotti, A.; Celestian, A.J.; Nilsson, M.; Hanson, G.N. A method for determining relative uranium concentrations in geological samples on a hand specimen scale. *Chem. Geol.* **2003**, *193*, 127–136. [CrossRef]
65. Llorens, I.; Solari, P.L.; Sitaud, B.; Bes, R.; Cammelli, S.; Hermange, H.; Othmane, G.; Safi, S.; Moisy, P.; Wahu, S.; et al. X-ray absorption spectroscopy investigations on radioactive matter using MARS beamline at SOLEIL synchrotron. *Radiochim. Acta* **2014**, *102*, 957–972. [CrossRef]
66. Roberts, N.M.W.; Rasbury, T.; Parrish, R.R.; Smith, C.J.; Horstwood, M.S.A.; Condon, D.J. A calcite reference material for LA-ICP-MS U-Pb geochronology. *Geochem. Geophys. Geosyst.* **2017**, *18*, 2807–2814. [CrossRef]
67. Paton, C.; Hellstrom, J.; Paul, B.; Woodhead, J.; Hergt, J. Iolite: Freeware for the visualisation and processing of mass spectrometric data. *J. Anal. At. Spectrom.* **2011**, *26*, 2508–2518. [CrossRef]
68. Woodhead, J.D.; Hellstrom, J.; Hergt, J.M.; Greig, A.; Maaß, R. Isotopic and Elemental Imaging of Geological Materials by Laser Ablation Inductively Coupled Plasma-Mass Spectrometry. *Geostand. Geoanal. Res.* **2007**, *31*, 331–343. [CrossRef]
69. Cao, W.; Xi, D.; Melinte-Dobrinescu, M.C.; Jiang, T.; Wise, S.W.; Wan, X. Calcareous nannofossil changes linked to climate deterioration during the Paleocene–Eocene thermal maximum in Tarim Basin, NW China. *Geosci. Front.* **2018**, *9*, 1465–1478. [CrossRef]
70. Roberts, N.M.W.; Drost, K.; Horstwood, M.S.A.; Condon, D.J.; Chew, D.; Drake, H.; Milodowski, A.E.; McLean, N.M.; Smye, A.J.; Walker, R.J.; et al. Laser ablation inductively coupled plasma mass spectrometry (LA-ICP-MS) U–Pb carbonate geochronology: Strategies, progress, and limitations. *Geochronology* **2020**, *2*, 33–61. [CrossRef]
71. Pickering, R.; Edwards, T.R. Factors controlling age quality in UPb dated Plio-Pleistocene speleothems from South Africa: The good, the bad and the ugly. *Chem. Geol.* **2021**, *579*, 120364. [CrossRef]
72. Passey, B.H.; Levin, N.E.; Cerling, T.E.; Brown, F.H.; Eiler, J.M. High-temperature environments of human evolution in East Africa based on bond ordering in paleosol carbonates. *Proc. Natl. Acad. Sci. USA* **2010**, *107*, 11245–11249. [CrossRef] [PubMed]
73. Henkes, G.A.; Passey, B.H.; Wanamaker, A.D.; Grossman, E.L.; Ambrose, W.G.; Carroll, M.L. Carbonate clumped isotope compositions of modern marine mollusk and brachiopod shells. *Geochim. Cosmochim. Acta* **2013**, *106*, 307–325. [CrossRef]
74. Gao, Y.; Henkes, G.A.; Cochran, J.K.; Landman, N.H. Temperatures of Late Cretaceous (Campanian) methane-derived authigenic carbonates from the Western Interior Seaway, South Dakota, USA, using clumped isotopes. *GSA Bull.* **2021**, *133*, 2524–2534. [CrossRef]
75. Dennis, K.J.; Affek, H.P.; Passey, B.H.; Schrag, D.P.; Eiler, J.M. Defining an absolute reference frame for "clumped" isotope studies of CO_2. *Geochim. Cosmochim. Acta* **2011**, *75*, 7117–7131. [CrossRef]
76. Brand, W.A.; Assonov, S.S.; Coplen, T.B. Correction for the ^{17}O interference in $\delta(^{13}C)$ measurements when analyzing CO_2 with stable isotope mass spectrometry (IUPAC Technical Report). *Pure Appl. Chem.* **2010**, *82*, 1719–1733. [CrossRef]
77. Petersen, S.V.; Defliese, W.F.; Saenger, C.; Daëron, M.; Huntington, K.W.; John, C.M.; Kelson, J.R.; Bernasconi, S.M.; Colman, A.S.; Kluge, T.; et al. Effects of Improved ^{17}O Correction on Interlaboratory Agreement in Clumped Isotope Calibrations, Estimates of Mineral-Specific Offsets, and Temperature Dependence of Acid Digestion Fractionation. *Geochem. Geophys. Geosyst.* **2019**, *20*, 3495–3519. [CrossRef]
78. Kim, S.-T.; O'Neil, J.R. Equilibrium and nonequilibrium oxygen isotope effects in synthetic carbonates. *Geochim. Cosmochim. Acta* **1997**, *61*, 3461–3475. [CrossRef]

79. Hill, C.A.; Polyak, V.J.; Asmerom, Y.; Provencio, P.P. Constraints on a Late Cretaceous uplift, denudation, and incision of the Grand Canyon region, southwestern Colorado Plateau, USA, from U-Pb dating of lacustrine limestone. *Tectonics* **2016**, *35*, 896–906. [CrossRef]
80. Hemingway, J.D.; Henkes, G.A. A disordered kinetic model for clumped isotope bond reordering in carbonates. *Earth Planet. Sci. Lett.* **2021**, *566*, 116962. [CrossRef]
81. Lan, Z.; Wu, S.; Roberts, N.M.W.; Zhang, S.; Cao, R.; Wang, H.; Yang, Y. Geochronological and geochemical constraints on the origin of highly $^{13}C_{carb}$-depleted calcite in basal Ediacaran cap carbonate. *Geol. Mag.* **2022**, *159*, 1323–1334. [CrossRef]
82. Lan, Z.; Roberts, N.M.; Zhou, Y.; Zhang, S.; Li, Z.; Zhao, T. Application of in situ U-Pb carbonate geochronology to Stenian-Tonian successions of North China. *Precambrian Res.* **2022**, *370*, 106551. [CrossRef]
83. Ludwig, K.R. Uranium-daughter migration and U/Pb isotope apparent ages of uranium ores, Shirley Basin, Wyoming. *Econ. Geol.* **1978**, *73*, 29–49. [CrossRef]
84. Sturchio, N.C.; Antonio, M.R.; Soderholm, L.; Sutton, S.R.; Brannon, J.C. Tetravalent Uranium in Calcite. *Science* **1998**, *281*, 971–973. [CrossRef]
85. Reeder, R.J.; Nugent, M.; Lamble, G.M.; Tait, C.D.; Morris, D.E. Uranyl Incorporation into Calcite and Aragonite: XAFS and Luminescence Studies. *Environ. Sci. Technol.* **2000**, *34*, 638–644. [CrossRef]
86. Choquette, P.W.; James, N.P. Diagenesis #12: Diagenesis in limestones—3: The deep burial environment. *Geosci. Can.* **1987**, *14*, 3–5.
87. Algeo, T.J.; Wilkinson, B.H.; Lohmann, K.C. Meteoric-burial diagenesis of Middle Pennsylvanian limestones in the Orogrande Basin, New Mexico: Water/rock interactions and basin geothermics. *J. Sediment. Petrol.* **1992**, *62*, 652–670.
88. Hasiuk, F.J.; Kaczmarek, S.E.; Fullmer, S.M. Diagenetic Origins of the Calcite Microcrystals That Host Microporosity in Limestone Reservoirs. *J. Sediment. Res.* **2016**, *86*, 1163–1178. [CrossRef]
89. Passey, B.H.; Henkes, G.A. Carbonate clumped isotope bond reordering and geospeedometry. *Earth Planet. Sci. Lett.* **2012**, *351–352*, 223–236. [CrossRef]
90. Stolper, D.A.; Eiler, J.M. The kinetics of solid-state isotope-exchange reactions for clumped isotopes: A study of inorganic calcites and apatites from natural and experimental samples. *Am. J. Sci.* **2015**, *315*, 363–411. [CrossRef]
91. MacDonald, J.M.; Faithfull, J.W.; Roberts, N.M.W.; Davies, A.J.; Holdsworth, C.M.; Newton, M.; Williamson, S.; Boyce, A.; John, C.M. Clumped-isotope palaeothermometry and LA-ICP-MS U–Pb dating of lava-pile hydrothermal calcite veins. *Contrib. Mineral. Petrol.* **2019**, *174*, 63. [CrossRef]
92. Vermeesch, P. Maximum depositional age estimation revisited. *Geosci. Front.* **2020**, *12*, 843–850. [CrossRef]
93. Platt, N.H.; Wright, V.P. Palustrine carbonates and the Florida Everglades; towards and exposure index for the fresh-water environment? *J. Sediment. Res.* **1992**, *62*, 1058–1071.
94. Freytet, P.; Verrecchia, E.P. Lacustrine and palustrine carbonate petrography: An overview. *J. Paleolimnol.* **2002**, *27*, 221–237. [CrossRef]
95. Alonso-Zarza, A.M.; Wright, V.P. Palustrine carbonates. *Dev. Sedimentol.* **2010**, *61*, 103–131.
96. Sheldon, N.D.; Tabor, N.J. Quantitative paleoenvironmental and paleoclimatic reconstruction using paleosols. *Earth-Sci. Rev.* **2009**, *95*, 1–52. [CrossRef]
97. Zhang, X.; Guo, J.; Wu, S.; Chen, F.; Yang, Y. Divalent heavy metals and uranyl cations incorporated in calcite change its dissolution process. *Sci. Rep.* **2020**, *10*, 16864. [CrossRef]
98. Banner, J.L.; Hanson, G.N. Calculation of simultaneous isotopic and trace element variations during water-rock interaction with applications to carbonate diagenesis. *Geochim. Cosmochim. Acta* **1990**, *54*, 3123–3137. [CrossRef]
99. Ahm, A.-S.C.; Bjerrum, C.J.; Blättler, C.L.; Swart, P.K.; Higgins, J.A. Quantifying early marine diagenesis in shallow-water carbonate sediments. *Geochim. Cosmochim. Acta* **2018**, *236*, 140–159. [CrossRef]
100. Galloway, J.M.; Hadlari, T.; Fensome, R.; Swindles, G.T.; Schroder-Adams, C.; Herrle, J.; Fath, J. Response of vegetation to Lower Cretaceous paleoclimate variation in the Canadian Arctic. In Proceedings of the EGU General Assembly Conference Abstracts, Vienna, Austria, 4–13 April 2018; p. 10324.
101. Li, J.; Wen, X.; Huang, C. Lower Cretaceous paleosols and paleoclimate in Sichuan Basin, China. *Cretac. Res.* **2016**, *62*, 154–171. [CrossRef]
102. Mutterlose, J.; Ruffell, A. Milankovitch-scale palaeoclimate changes in pale–dark bedding rhythms from the Early Cretaceous (Hauterivian and Barremian) of eastern England and northern Germany. *Palaeogeogr. Palaeoclim. Palaeoecol.* **1999**, *154*, 133–160. [CrossRef]